This article was downloaded by:
On: *21 January 2011*
Access details: *Access Details: Free Access*
Publisher *Taylor & Francis*
Informa Ltd Registered in England and Wales Registered Number: 1072954 Registered office: Mortimer House, 37-41 Mortimer Street, London W1T 3JH, UK

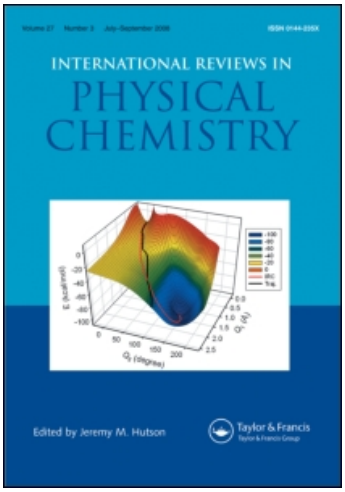

International Reviews in Physical Chemistry
Publication details, including instructions for authors and subscription information:
http://www.informaworld.com/smpp/title~content=t713724383

Electron-driven chemistry of halogenated compounds in condensed phases: Effects of solvent matrices on reaction dynamics and kinetics

C. C. Perry[a]; N. S. Faradzhev[b]; D. H. Fairbrother[a]; T. E. Madey[b]
[a] Department of Chemistry, Johns Hopkins University, Baltimore, MD 21218, USA [b] Department of Physics and Astronomy, and Laboratory for Surface Modification, Rutgers, The State University of New Jersey, Piscataway, NJ 08854-8019, USA

To cite this Article Perry, C. C. , Faradzhev, N. S. , Fairbrother, D. H. and Madey, T. E.(2004) 'Electron-driven chemistry of halogenated compounds in condensed phases: Effects of solvent matrices on reaction dynamics and kinetics', International Reviews in Physical Chemistry, 23: 2, 289 — 340
To link to this Article: DOI: 10.1080/01442350412331284625
URL: http://dx.doi.org/10.1080/01442350412331284625

PLEASE SCROLL DOWN FOR ARTICLE

Full terms and conditions of use: http://www.informaworld.com/terms-and-conditions-of-access.pdf

This article may be used for research, teaching and private study purposes. Any substantial or systematic reproduction, re-distribution, re-selling, loan or sub-licensing, systematic supply or distribution in any form to anyone is expressly forbidden.

The publisher does not give any warranty express or implied or make any representation that the contents will be complete or accurate or up to date. The accuracy of any instructions, formulae and drug doses should be independently verified with primary sources. The publisher shall not be liable for any loss, actions, claims, proceedings, demand or costs or damages whatsoever or howsoever caused arising directly or indirectly in connection with or arising out of the use of this material.

INT. REVIEWS IN PHYSICAL CHEMISTRY, 2004
VOL. 23, NO. 2, 289–340

Taylor & Francis
Taylor & Francis Group

Electron-driven chemistry of halogenated compounds in condensed phases: Effects of solvent matrices on reaction dynamics and kinetics

C. C. PERRY†, N. S. FARADZHEV‡, D. H. FAIRBROTHER† and T. E. MADEY‡*

†Department of Chemistry, Johns Hopkins University, Baltimore, MD 21218, USA

‡Department of Physics and Astronomy, and Laboratory for Surface Modification, Rutgers, The State University of New Jersey, Piscataway, NJ 08854-8019, USA

The focus of this review is the effect of H_2O on the electron-driven chemistry of condensed halogenated compounds. We present data with emphasis on results from the authors' laboratories for halomethanes (CF_2Cl_2, CCl_4, CH_3I, $CDCl_3$, CD_2Cl_2) and SF_6. The halogenated species are suspended in or adsorbed on the surface of ultrathin films of amorphous solid water (ice) condensed on metal surfaces. Bombardment of the film by X-rays or energetic electrons leads to the release of low-energy secondary electrons; these are responsible for much of the rich electron-driven chemistry, which includes molecular decomposition, desorption of charged and neutral fragments, radical formation, anion solvation, and condensed-phase reactions. Potential implications of this work range from environmental remediation of toxic compounds to atmospheric ozone depletion.

Downloaded At: 16:25 21 January 2011

Contents

*Corresponding author. E-mail: madey@physics.rutgers.edu

International Reviews in Physical Chemistry ISSN 0144–235X print/ISSN 1366–591X online © 2004 Taylor & Francis Ltd
http://www.tandf.co.uk/journals
DOI: 10.1080/01442350412331284625

Downloaded At: 16:25 21 January 2011

Downloaded At: 16:25 21 January 2011

1. Introduction

Electron-driven processes (EDPs) [1–5] are important in many diverse areas, including environmental remediation [6], semiconductor processing, radiobiology and biochemistry [7]. For example, electron-stimulated processes are important in radiation therapy where low-energy secondary electrons (<5 eV) generated by the irradiation source are believed to induce DNA strand breakage [8]. The possible influence on atmospheric ozone depletion of low-energy secondary electrons released by cosmic rays in collisions [9] with ice particles in polar stratospheric clouds (PSCs) is also a subject of extensive discussion [10–12]. EDPs can occur for molecules in both gas and condensed phases. In the gas-phase, examples of EDPs include plasma and high-energy remediation of environmental pollutants [6, 13], as well as reactions that occur in atmospheric [14] and interstellar chemistry [15]. EDPs in condensed-phase environments include nanolithography [16] and radiation processing of toxic chemicals [17]. Indeed, the diversity of media where EDPs are prevalent accounts for the study of electron-stimulated processes in experiments that range from molecular beam scattering to surface photochemistry. Despite the presence of extensive literature in the area of EDPs [1–3], the complexity of the reactions means that there are still significant gaps in our understanding of the fundamental charge and energy transfer processes. This is especially true for EDPs in complex systems involving molecules present in water and other aqueous solvents.

The scope of this review is the radiation-induced decomposition and chemistry of ultrathin films (~1–100 ML) containing halogenated compounds (i) adsorbed on metal surfaces and (ii) co-deposited in water (ice) films. Measurements are made using ultrahigh vacuum surface-sensitive analytical probes and most examples are taken from recent work in the authors' laboratories. Particular emphasis is on the roles of water ice matrices and low-energy electrons in EDPs of halogen-containing compounds. The results presented here have significance in plasma and high-energy remediation of organohalides along with potential implications for chemistry and physics pertinent to the earth's upper atmosphere.

In the condensed phase, electron-stimulated processes can be broadly categorized as occurring from the primary beam (electrons or photons) or via low-energy secondary electrons. Irrespective of the primary irradiation source, low-energy electrons play dominant roles in all aspects of radiation damage in solids and liquids [18]. During bombardment of solids by many forms of high-energy radiation (electrons, ions, photons), a cascade of low-energy secondary electrons (0–100 eV) accompanies the radiation–solid interactions; these low-energy electrons are particularly effective in initiating bond-breaking processes [19]. Indeed, the non-thermal dissociation of condensed molecules by low-energy electron excitation is a major factor in radiation-induced modification of condensed matter.

Detailed studies of EDPs in the condensed phase have become increasingly prevalent over the past decade [20, 21]. One of the most useful approaches for studying EDPs has been to carry out measurements under ultrahigh vacuum conditions where a wide range of surface and gas-phase analytical techniques can be used to interrogate different aspects of the overall EDPs, including the detection and characterization of neutral and charged species in the gas phase and the associated chemical transformations within the film [22].

Electron-stimulated decomposition is a particularly important and efficient process for halogenated compounds. This has been ascertained through numerous spectroscopic studies that have identified electronic states (resonances) along with

their associated lifetimes [20, 23]. Different experiments have been performed to measure the energy dependence of cross-sections involved in the elastic, inelastic, ionizing and dissociative processes induced by the interaction of low-energy electrons with halogenated compounds [20, 23–25]. Studies of EDPs for halogenated compounds have also been motivated by their relevance as electron sinks in situations where it is necessary to extinguish flames, plasmas or arcs. Similarly, the electron-stimulated reactions of organohalides in plasma discharges have been investigated as a remediation technology [26].

There is extensive literature on the electron-driven decomposition of gaseous and condensed-phase organohalides, and the basic EDPs for organohalides such as CCl_4 and CF_2Cl_2 are well understood [27–34]. Although the 'neat' condensed films have been well studied, much less is understood concerning the role of matrix effects involving polar molecules (mainly water). There are reports [32, 35] (see section 3) that when organohalides are condensed with water ice, that is under conditions where the formation and diffusion of fully solvated electrons is much slower than dissociation times, the electron-induced dissociation of halogenated compounds occurs with higher cross-sections than are seen for 'neat' condensed films. This could have implications for atmospheric ozone depletion processes that involve species such as CF_2Cl_2, whose electron-stimulated decomposition may generate stratospherically important species such as carbon dioxide and/or carbonyl dihalides ($COCl_2$, COF_2, COFCl); these species may undergo subsequent photodissociation, yielding haloformyl radicals (XCO) and halogen atoms. However, in these systems, many questions remain about reaction mechanisms, the role of precursor electrons, solvated electrons and other reactive species formed as the result of H_2O radiolysis, as well as the direct identification of decomposition products and dissociation cross-sections. Despite the importance of organohalides in atmospheric chemistry, the role of EDPs in atmospheric ozone depletion is controversial [12] and, until recently, has been assumed to be minor based on the low abundance of stratospheric free electrons [10].

The aim of this review is to highlight the rich chemistry and physics that occur in the EDPs for a series of small halogenated compounds adsorbed on metal substrates and co-deposited with water (ice) in ultrathin films; ultrahigh vacuum surface science methods are used throughout. Our results are compared and contrasted with recent literature reports of large enhancements in rates of EDPs for halocarbons co-deposited with water (ice). In particular, we present evidence that co-adsorption with water (ice) has a relatively small effect on the cross-sections for electron-induced decomposition of organohalides. We discuss our *direct* measurements of dissociation cross-sections in the framework of water-enhanced organohalide dissociation rates based on *indirect* measurements of anion electron-stimulated desorption and charge trapping.

The review is organized in the following way. In the next section, we provide a brief description of the surface and gas-phase analytical techniques that were used in these studies with particular emphasis on the complimentary molecular level information that each particular technique can provide. In section 3 we summarize the characteristics of electron attachment processes in the gas and condensed phases for halocarbons. In particular, we contrast the dynamics and reactivity of organohalides on going from the gas to the condensed phase. Section 4 details experimental results obtained on the electron-driven chemistry and dynamics of halocarbons adsorbed on metal surfaces and with water (ice) films. In section 5 we provide

Downloaded At: 16:25 21 January 2011

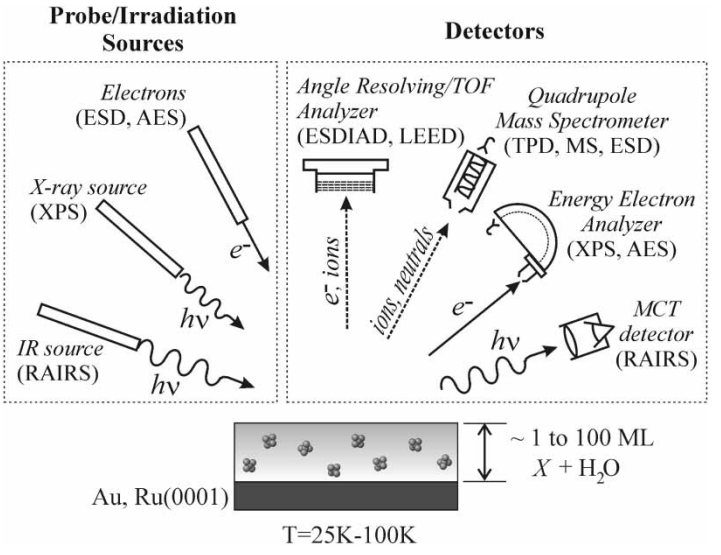

Figure 1. Schematic of our experimental UHV set-ups designed for characterization of surface structure and reaction dynamics. The techniques used are: mass spectroscopy (MS), temperature-programmed desorption (TPD), electron-stimulated desorption (ESD) of positive/negative ions and neutrals (using a QMS detector), electron-stimulated desorption ion angular distribution (ESDIAD) for positive/negative ions (using the TOF technique), X-ray photoelectron spectroscopy (XPS), reflection absorption infrared spectroscopy (RAIRS), Auger electron spectroscopy (AES) and low-energy electron diffraction (LEED). The film $X+H_2O$ represents a halocarbon (X) co-adsorbed with water on a metal surface.

Downloaded At: 16:25 21 January 2011

mechanistic interpretations and discuss implications of these studies. The article concludes in section 6, with some ideas and thoughts about possible future directions of electron-driven reactions at surfaces and in thin films.

2. Experimental details

The experiments that are the focus of this article were carried out in three different ultrahigh vacuum (UHV) systems [36–41]. Figure 1 represents the schematic of a virtual (generalized) set-up that illustrates the instrumentation used in these chambers for characterization of the surface structure, composition and reactivity of thin films containing halogenated compounds.

Two major groups of surface-sensitive techniques are used for characterization of radiation-stimulated chemistry in adsorbed layers and condensed films. The first group is sensitive to species (reactants and products) remaining on the surface or trapped in the film at low temperatures (25–100 K). This includes X-ray photoelectron spectroscopy (XPS) and Auger electron spectroscopy (AES). They provide quantitative information on the relative concentration of elements on the surface as well as chemical information derived from core-level binding energy shifts. Reflection absorption infrared spectroscopy (RAIRS) also provides chemical information based on the identification of characteristic vibrational frequencies that enable us to identify specific functional groups and molecular products. The complementary nature of these techniques allows us to develop a more complete

picture of the chemical transformations induced by low-energy electrons. For example, XPS can distinguish between different chemical bonding environments (e.g. C–Cl and Cl^-), while RAIRS can unambiguously identify new molecular products (e.g. CO_2, H_3O^+).

The second group of techniques is used to detect species (ions and neutrals) that desorb from the surface either thermally or under irradiation. This group includes mass spectroscopy (MS) methods: electron-stimulated desorption (ESD) of positive/negative ions and neutrals for mass-resolved analysis of species desorbing from the surface under electron bombardment; temperature-programmed desorption (TPD) for determination of neutrals (both reactants and products) thermally desorbed from the surface; and also time-of-flight (TOF) electron-stimulated desorption ion angular distribution (ESDIAD), which supplies information about intensities and spatial distributions of desorbing positive/negative ions and provides insights into the local structure and the bonding geometry of adsorbed molecules. An additional technique, low-energy electron diffraction (LEED), is used for the determination of long-range surface order.

The MS techniques (TPD and ESD) are based on commercially available quadrupole mass spectrometers while the XPS system is equipped with a multi-channel hemispherical analyser. The apparatus for AES uses a 50 mm concentric hemispherical analyser (CHA) and a Kimball Physics electron gun; AES is used in our experiments predominantly for analysis of substrate cleanliness. The RAIRS arrangement is equipped with a Mattson Infinity series FTIR spectrometer. The ESDIAD detector is used to measure angular distributions of desorbed positive and negative ions, and has TOF capability for mass-resolved ion detection. The details of these techniques have been reported elsewhere [36, 40, 41].

Downloaded At: 16:25 21 January 2011

All measurements were made under UHV conditions. The substrates included polycrystalline Au foils and a Ru single crystal. The Ru(0001) sample was mounted on an XYZ-rotary manipulator. A closed-cycle helium refrigerator allowed for the cooling of the crystal to 25 K. The substrate could be heated to 1600 K. The polycrystalline Au substrates used for RAIRS and XPS were mounted on a Ta holder that was cooled to ~100 K. The samples were cleaned by Ar^+ sputtering. The Ru single crystal was also cleaned by heating in oxygen, followed by annealing in vacuum. Surface cleanliness and structure were monitored either by AES and LEED or by XPS.

In radiation-damage experiments, the Mg Kα anode (1253.6 eV) operating at 300 W (15 kV) was used as a source of X-rays. A low-energy flood gun (Specs 15/40) or an unshielded QMS filament was used as a source of electrons with broad and nearly uniform spatial distribution and kinetic energy of ~200 eV. For the ionic ESD and ESDIAD measurements described in sections 4.1, 4.2 and 4.4, the surface was bombarded by a focused electron beam from a Kimball Physics electron gun operating in a pulsed mode (for TOF studies) at energies of 250–350 eV and average beam current ~0.1 nA. All other irradiation (X-ray, electrons) experiments described in this article were performed in continuous mode.

In all experiments, high-purity gases ($^{12}CF_2Cl_2$, $^{12}CCl_4$, $^{13}CCl_4$, $^{12}CDCl_3$, $^{12}CD_2Cl_2$, $^{12}CH_3I$, SF_6, H_2O and D_2O) were supplied by Matheson, Aldrich, Millipore or Cambridge Isotopes. The gases were stored in separate vacuum vessels attached to a gas manifold. The purity of gases introduced into a chamber was checked by mass spectrometry. The gases were dosed onto the substrate either from background (at 100 K in the RAIRS/XPS system) or directly from a microcapillary

array doser aimed normally to the surface (at 25 K in the TPD/ESD system). All elemental XP spectra were charge calibrated from either the Cl^- $2p_{3/2}$ or C–Cl $2p_{3/2}$ peaks within the Cl 2p spectral envelope, centred at 198 and 201 eV, respectively [42]. The film composition and the thickness were monitored by XPS (in the RAIRS/XPS system) or by TPD (in the TPD/ESD system). For mixed halocarbon/water films, the chemical composition of the film was determined using XPS or TPD, and defined in terms of the halocarbon: water ratio [36]. Dilute and concentrated films had halocarbon: water ratios of <0.1 and >0.3, respectively.

3. Background

3.1. *Interaction of low-energy electrons with gas-phase halocarbons*

A non-thermal EDP resulting in efficient dissociation of halogenated compounds (including CFCs) is resonant electron capture leading to dissociative electron attachment (DEA). In DEA, a low-energy electron (0 to ~10 eV) collides with a molecule to form a vibrationally or electronically excited transient negative ion state. If the lifetime of this state is comparable to the vibrational period of the bond (e.g. $>10^{-14}$ s), the transient negative ion can dissociate into energetic neutral and anionic fragments:

$$\begin{aligned} e^- + AB \rightarrow (AB)^{*-} &\rightarrow A + B^- \\ &\rightarrow A^- + B \end{aligned} \quad (1)$$

For gaseous halogenated molecules, DEA is an efficient process with cross-sections that exceed 10^{-16} cm^2 for CF_2Cl_2, $CHCl_3$ and CCl_4 at near 0 eV electron energies [43–45]. For this series of halogenated compounds, the cross-sections for DEA near 0 eV increases as the Cl content in the molecule increases.

For gaseous CF_2Cl_2, electron-mediated dissociation at energies <15 eV is dominated by DEA, and the integrated Cl^- yield as a function of incident energy (<15 eV) is about $10\times$ the F^- yield, indicating that the dominant reaction channel involves C–Cl bond cleavage, producing Cl^- as the most abundant anion fragment [24, 44, 46, 47]. As the C–Cl bond dissociation energy is smaller than the electron affinity of Cl the DEA reaction

$$e^- + CF_2Cl_2 \rightarrow CF_2Cl_2^{*-} \rightarrow \cdot CF_2Cl + Cl^- \quad (2)$$

is exoergic by ~0.28 eV at an electron energy of ~0 eV [44]. There are at least five negative ion resonant states whose energies lie above the zero-energy level [44, 48]; their average energies are 0.9, 2.5, 3.5, 6.2 and 8.9 eV. For higher incident energies ($\geq$15 eV) dipolar dissociation (DD), where the parent molecule dissociates into stable anionic and cationic species, becomes important [49].

In DEA of gaseous CCl_4 by 0–10 eV electrons, the most intense ion fragment is Cl^-, by several orders of magnitude [50]. There is a sharp Cl^- feature with a cross-section approaching 5×10^{-13} cm^2 near 0 eV, and a second maximum at 0.8 eV [51]. The DEA process

$$e^- + CCl_4 \rightarrow CCl_4^{*-} \rightarrow \cdot CCl3 + Cl^- \quad (3)$$

is exoergic by ~0.45 eV at an electron energy of 0 eV [51, 52]. The electron-stimulated reactions of both CH_2Cl_2 and $CHCl_3$ in the gas phase have also been studied. In both cases, Cl^- is the dominant anion fragment formed at electron energies $\leq$10 eV. Chloride anion yields are found with an onset at ~0 eV with DEA cross-sections

Downloaded At: 16:25 21 January 2011

for CH_2Cl_2 $<10^{-17}\,cm^2$ [43, 53] and for $CHCl_3$, $\sim 1\times10^{-15}\,cm^2$ [51, 54]. Similarly, for gas-phase CH_3I a resonance at $\sim$0.17 eV is observed for I^- with a cross-section of $5.8\times10^{-15}\,cm^2$ [55].

SF_6 is an environmentally important molecule that contributes to global warming as a greenhouse gas. The ability to capture thermal electrons makes SF_6 widely used for technical applications as an electron scavenger in high-voltage electrical devices [56]. SF_6 is also used as a dry-etching gas in plasma processing [57]. Electron bombardment of gaseous SF_6 leads to the formation of both positive and negative ions. SF_6^- is formed via attachment of very low-energy electrons ($\leq$0.2 eV) while SF_5^- is the dominant product of DEA, and is formed at electron energies of 0.3$^-$1.5 eV. The maximum cross-section for SF_5^- production is reported to be $2\times10^{-16}\,cm^2$ for electron energies between $\sim$0.1 and 0.5 eV [58]. A low-energy DEA resonance of SF_6 also leads to F^- formation. The corresponding reaction is:

$$e^- + SF_6 \rightarrow SF_6^{*-} \rightarrow F^- + \cdot SF_5 \quad (4)$$

Other anions detected are F_2^- and SF_n^- ($n=1$–4) [59].

Electron-induced dissociation of SF_6 leading to the formation of positive ions becomes significant above $\sim$16 eV, producing SF_x^+ ($x=1,3,4,5$) and F^+ [58]. Measurements of electron impact dissociative ionization of gaseous SF_6 gave the threshold energy for F^+ formation at $\sim$30 eV [60].

In summary, these gas-phase studies demonstrate that dissociative attachment of low-energy electrons is the dominant decomposition mechanism for halogenated molecules characterized by low-energy resonances near $\sim$0 eV.

3.2. *Reactions of low-energy electrons with organohalides adsorbed on solid surfaces and in condensed phases*

DEA processes have been studied extensively in the condensed phase by the groups of Sanche and Illenberger [61, 62]. Typically, these studies have involved identification of the intermediate anion states, energy dependencies, yields and cross-sections. For halocarbons adsorbed on solid substrates, decomposition can be initiated by a range of irradiation sources (photons, high-energy particles) either by direct excitation or indirectly via secondary electrons. Direct processes, including photodissociation (in which the incident photon energy is absorbed by a molecule) as well as DEA, dipolar dissociation (DD) or dissociative ionization (DI), are induced by the primary electron beam interacting with a molecule. Indirect processes, including DEA, DD, etc., are induced by secondary electrons released from the substrate or the condensed film. For example, it has been recognized that photochemical reactions induced by UV photons of halocarbons adsorbed on metal surfaces are often controlled by photoinduced electron transfer from substrate to adsorbate, which can lead to DEA [2, 63, 64] (an indirect process). Upon the formation of multilayers, however, direct photodissociation induced by UV photons becomes increasingly dominant because the DEA channel is quenched by the finite penetration depth of the substrate-generated low-energy photoelectrons [65]. This was illustrated in a recent photochemical study on methyl chloride *multilayer* water (ice) films by Lilach and Asscher [66]. They attempted to distinguish TPD products generated via the DEA mechanism (CHD_3, C_2D_6 and HD) from those formed via direct photodissociation (HOCl and CD_3CD_2Cl) using water spacer experiments. In related studies by Yabushita *et al.* [67], the photodissociation dynamics in Cl_2/water (ice) and $CFCl_3$/water (ice) films were measured from TOF spectra using

Downloaded At: 16:25 21 January 2011

resonance-enhanced multiphoton ionization (REMPI). Their results show that fragmentation into radicals occurs at the initial stage of halocarbon dissociation (e.g. Cl/Cl* from $CFCl_3$ irradiated by UV vs. Cl^- from CF_2Cl_2 dissociated by electrons). These studies illustrate that the reaction channels available are dependent upon the excitation mechanism.

The detailed dynamics of DEA processes involving condensed-phase organohalides [19, 61] are often modified when compared to analogous studies in the gas phase. For example, there have been a number of studies detailing negative ion desorption from condensed-phase CF_2Cl_2 [68, 69]. In contrast to gas-phase studies on CF_2Cl_2, there is general agreement that the total yield of ejected F^- ions during low-energy electron excitation of condensed CF_2Cl_2 considerably exceeds the Cl^- yield [70]. This difference is attributed to the low kinetic energies of Cl^- ions, which results in the majority of the Cl^- ions remaining trapped on the surface as they have insufficient kinetic energies to overcome the polarization barrier. For positive ions, the dominant gas-phase species produced during electron-stimulated reactions of condensed CF_2Cl_2 over a wide range of electron energies (~40 to >200 eV) include CF_2Cl^+, Cl^+ and F^+ [71].

Electron bombardment of CF_2Cl_2 co-adsorbed with polar molecules (e.g. NH_3, H_2O) has been observed to result in an increase in the anion ESD yield, an effect ascribed to an increased charge trapping coefficient [30, 32, 70]. Thus, Lu and Madey discovered that co-adsorption of CF_2Cl_2 with H_2O on a Ru(0001) substrate leads to a $\sim 100\times$ enhancement of Cl^- ion yields in electron-stimulated desorption, compared to the yield from CF_2Cl_2 adsorbed alone [14, 30]. Moreover, Lu and Sanche have also reported a large increase in the charge trapping coefficient [30, 32, 70] of CF_2Cl_2 co-adsorbed with H_2O [46]. This was ascribed to an increase in the DEA cross-section of CF_2Cl_2: $\sigma = 1.3 \times 10^{-14}\,cm^2$ vs. $\sigma = 1.4 \times 10^{-15}\,cm^2$ in the absence of co-adsorbed H_2O. These enhancements have been attributed to an electron-trapping mechanism by the polar molecule, which increases the probability of DEA. As we discuss later in section 5.3, this interpretation is not unambiguous, and direct measurements of halocarbon dissociation cross-sections discussed in this review article reveal, at most, a weak dependence on the presence or absence of water (ice).

The effects of polar liquids on electron-stimulated processes have been discussed in terms of the properties of electrons in these polar media. Thus, an electron travelling through a polar liquid such as water can lose its energy and become trapped [72]. Indeed, the properties of electrons trapped in polar media are a topic of current scientific debate due to their importance in a wide range of EDPs [1]. It is generally accepted that a solvated electron, e_{aq}, is responsible for chemical bond-breaking in liquid water solutions, forming halide ions in aliphatic compounds containing Cl, Br or I [3, 4]. However, in fluorocarbons such as C_6F_6, C_6H_5F, CF_4, etc., where a few eV of electronic excitation is needed for DEA, the solvated electron is too low in energy to initiate dissociation directly. In these systems 'hot' pre-solvated electrons may be responsible for DEA processes.

3.3. *Structure of water (ice) films*

In condensed-phase experiments, similar to those discussed in section 3.2, halogenated molecules and water are co-deposited on the substrate at low temperature. The condensation of multilayers of water at low temperatures (~100 K) results in the formation of amorphous solid water (ASW) (ice) [73–75].

Downloaded At: 16:25 21 January 2011

ASW is the most abundant phase of water in astrophysical environments such as comets, planetary rings and interstellar clouds [9]. Extensive experimental and theoretical studies indicate that ASW grown by depositing water via background dosing under UNV conditions at substrate temperatures < 120–130 K produces an amorphous microporous structure, which is metastable with respect to crystalline ice [76]. By contrast, background water deposition above 120–130 K results in the formation of pore-free solid ice [77]. The influence of dosing conditions upon the microstructure of ice has been studied by Smith and Kay using an effusive beam source [78]. These studies reveal that pore-free ASW films can be grown as low as 22 K if a well-collimated H_2O vapour beam at normal incidence is used for deposition; however, at off-normal or under background dosing conditions, highly porous ice films result from water deposition at 22 K. As mentioned in section 2, films described here were prepared using both background dosing at 100 K and normal beam dosing at 25 K, and thus had porous and non-porous ASW structures, respectively. Throughout this paper, we express H_2O coverages as monolayers (ML) on Ru and Au surfaces, where one ML corresponds to the density of H_2O molecules in one ideal bilayer on Ru(0001), $1.05 \times 10^{15}\,cm^{-2}$ [79].

3.4. *Electron-stimulated reactions in water (ice)*

Downloaded At: 16:25 21 January 2011

The interaction of ionizing radiation with water and water (ice) has received a considerable amount of recent scientific interest due, in large part, to the importance of understanding radiation-induced transformations in biological systems and astrophysical environments. It is well known that the interaction of energetic radiation (electromagnetic radiation, electron beams) with water generates cations, anions and radicals primarily through ionization, DEA and dissociative excitation, respectively [5]. The principal reactive species produced during the interaction of ionizing radiation and electrons with water are thought to include solvated electrons, hydroxyl radials and hydrogen atoms [80]. However, the branching ratios of these reactive intermediates are only understood at a rudimentary level. In addition, the excited state dynamics are expected to depend on temperature, the structural form of the water (ice), and the presence of solutes and interfaces [5].

The nature of reaction products and their associated internal energy distributions produced during the interaction of low-energy (< 200 eV) electrons with water (ice) films has been the subject of a number of recent studies by Orlando and co-workers [81–83]. Neutral gas-phase products have been detected during the interaction of < 200 eV electrons with amorphous D_2O (D-ice) that include atomic D and O, as well as D_2 and O_2 [82, 83]. Recently, it has been demonstrated that the O_2 yield is dependent upon the phase and temperature of the water (ice) film and that the formation of O_2 is dominated by excitation and dissociation of a stable precursor, rather than diffusion and recombination of oxygen atoms [83, 84]. In addition, there is a distinct incident energy threshold of 10 ± 2 eV for O_2 formation [83]. This threshold was assigned to the ionization or valence-level electronic excitations of condensed water molecules. In a related study, the electron-stimulated production of D_2 from amorphous solid D_2O was found to occur at substrate/water (ice) and ASW/vacuum interfaces, but not in the bulk [85]. In similar studies, Prince *et al.* [86] reported that excited $^{\cdot}OH$ radicals were produced during the interaction of 15–50 eV electrons with ice, while Noell *et al.* [87] reported the production of H^+ above 21 eV.

In contrast to electron-stimulated reactions in aqueous media, 'cage effects', which refer to species trapped in an ice matrix, are likely to have an important

role in electron-stimulated reactions in condensed water (ice) phases. For example, vastly different time-scales for molecular motion between ASW and liquid water will affect such critical processes as the length scales of diffusion and electron solvation.

In section 3.1 we compared different gas-phase electron-driven studies of various halogenated compounds (CF_2Cl_2, CCl_4, $CHCl_3$, CH_2Cl_2 and CH_3I), contrasting their resonances and cross-sections. We presented illustrative examples in section 3.2 of electron-beam studies initiated by exposure of low-energy electrons to condensed 'neat' halomethanes. In sections 3.3 and 3.4, we summarized studies that are directed towards understanding both the structural and chemical aspects of EDPs in water.

4. Results

The focus of this review article is the kinetics of electron-stimulated reactions of halocarbons on metals, and of mixed-component condensed halocarbon/water (ice) systems. By using such films, we demonstrate how surface science techniques such as RAIRS, XPS, ESDIAD and TPD can probe the interaction between reactive species produced in these mixed component systems during their exposure to low-energy electrons.

Downloaded At: 16:25 21 January 2011

4.1. *Orientation and bonding geometry of SF_6 and CF_2Cl_2 on Ru(0001)*

The surface of a single crystal represents a periodic array of atoms that in many cases can serve as a template for an ordered adsorbed layer. ESDIAD is a very useful technique for studying the structure and the local bonding geometry of molecules adsorbed on surfaces [21, 88]. In an ESD process, bond breaking leads to ejection of an energetic ion or atom on a trajectory determined by the ground state bond direction. That is, the initial repulsive interaction is directed along the broken bond; energetic ions (atoms) are expelled and their trajectories provide information about molecular bonding geometry (note that ion trajectories are also influenced by image charge and reneutralization effects). Our ESDIAD experiments include measurements of the angular distributions of both positive and negative ions, from which we infer the bonding geometry of the adsorbed molecules. For illustration in the following discussion, we consider the adsorption and bonding geometry of two halogen-containing species, SF_6 and CF_2Cl_2.

The azimuthal orientations of S–F bonds for SF_6 adsorbed on Ru(0001) at 25 K have been established by ESDIAD [40, 41]. After deposition of submonolayer coverages of SF_6, strong off-normal emissions of both F^+ and F^- ions are observed. A typical 'halo' pattern for F^+ ions is shown in figure 2(a). A similar pattern is detected for F^- ions. Heating the adsorbed SF_6 layer transforms the ESDIAD patterns for both F^+ and F^- ions. As the temperature approaches $\sim$90 K, the initial 'halos' are replaced by distinct sixfold symmetry patterns for both ions (F^+ in figure 2(b) and F^- in figure 2(c)).

The pattern in figure 2(a) indicates that SF_6 molecules adsorb on Ru(0001) at 25 K by three fluorine atoms with the other three S–F bonds pointing away from the surface (figure 2(d)) in off-normal directions. The molecules have random azimuthal orientations that lead to 'halo'-like ESDIAD patterns. Heating the sample induces a rearrangement and ordering of the molecules that results in the hexagonal patterns seen in figures 2(b) and 2(c). The existence of six beams in these figures is attributed to the adsorption of SF_6 in two domains on Ru(0001) with opposite azimuthal orientation. The central beam exists only for F^+ ions (figure 2(b)) and is due to ESD

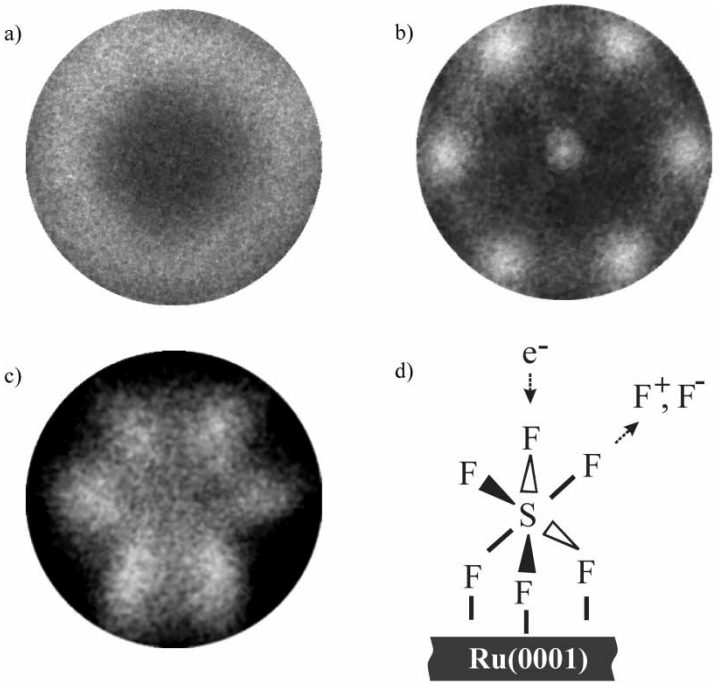

Figure 2. ESDIAD patterns for desorption of F^+ (a, b) and F^- (c) from 0.6 ML of SF_6 on Ru(0001) at 25 K. Pattern (a) corresponds to 'as deposited', and patterns (b) and (c) are seen after heating to 90 K. All measurements are made at 25 K. Electron energy is 350 eV for F^+ ions and 250 eV for F^- ions. Sketch (d) illustrates adsorption of SF_6 on Ru(0001) by three F atoms and indicates the rupture of the S–F bond under electron bombardment and desorption of F^+ and F^- ions in the off-normal direction. The patterns are reproduced from ref. [41]. All ESDIAD patterns are shown in a linear grey scale where the white colour corresponds to the maximum ion desorption intensity. These patterns represent two-dimensional spatial distributions of desorbing ions projected onto a planar detector.

Downloaded At: 16:25 21 January 2011

from a thermal decomposition product of SF_6, either chemisorbed F or another fragment with an S–F bond perpendicular to the surface. Electron beam exposures higher than $10^{14}\,cm^{-2}$ lead to formation of SF_x ($x = 0$–5) fragments, which become the source of positive ions in normal and off-normal directions [40]; exposures $>10^{16}\,cm^{-2}$ result in decomposition of the entire adsorbed SF_6 layer.

Figure 3(a) shows an ESDIAD pattern for F^- ions from a fractional monolayer of CF_2Cl_2 deposited at 25 K on the same substrate. A similar pattern is observed for Cl^-. The pattern exhibits only a broad central beam. CF_2Cl_2 has a tetrahedral configuration, in contrast to the octahedral SF_6 molecule. Thus, the ESDIAD pattern of figure 3(a) leads us to conclude that CF_2Cl_2 also adsorbs on hexagonally symmetric Ru(0001) by three halogens (either by 2F+1 Cl or by 2Cl+1F) with a single C–X bond (X=F, Cl) pointing away (figure 3(b)). This C–X bond is oriented along the surface normal, and when ruptured it leads to a central-beam ESDIAD pattern with the broadening due to thermal vibrations of the molecule. No heating-induced change in the patterns has been detected, suggesting that the bonding geometry does not change prior to the onset of desorption.

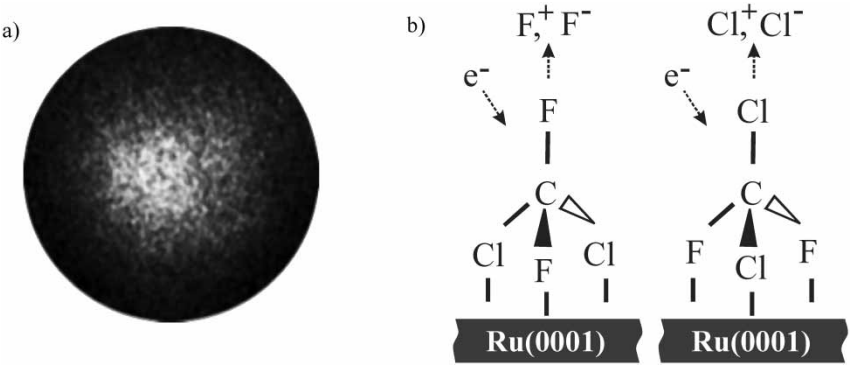

Figure 3. ESDIAD pattern (a) for desorption of F^- from 0.6 ML of CF_2Cl_2 adsorbed on Ru(0001) at 25 K. Electron energy is 250 eV. Sketch (b) illustrates two possible orientations of CF_2Cl_2 on Ru(0001) surface with the C–F bond (left) or C–Cl bond (right) oriented perpendicular to the surface. This indicates the rupture of the bonds under electron bombardment and desorption of F^+, F^- ions (or Cl^+, Cl^-) normal to the surface. All ESDIAD patterns are shown in a linear grey scale where the white colour corresponds to the maximum ion desorption intensity. These patterns represent two-dimensional spatial distributions of desorbing ions projected onto a planar detector.

Downloaded At: 16:25 21 January 2011

ESDIAD measurements provide us with strong evidence of the adsorption geometry of both SF_6 and CF_2Cl_2 on Ru(0001); the molecules are adsorbed on the hexagonal Ru surface via three halogen atoms. Although the data for CF_2Cl_2 do not indicate the orientation of the C–X bonds (X=F, Cl) in the plane of the surface, SF_6 measurements testify to the random azimuthal orientation of S–F bonds following adsorption at 25 K, and to irreversible ordering of SF_6 in two complementary domains upon heating.

4.2. *F^- and Cl^- ESD from CF_2Cl_2 co-adsorbed with water on Ru(0001)*

Electron bombardment promotes desorption of energetic neutral/ionic fragments from the surface. The 'side effect' of electron-induced desorption involves altering the bonding of surface species, initiating their decomposition. This can result in formation of free radicals and ionic species that may undergo subsequent chemical reactions on the surface [2, 63]. Anion ESD yields can be changed dramatically by co-adsorption of CF_2Cl_2 with highly polar molecules such as water. Several experiments have reported that ESD anion yields from PF_3 and CF_2Cl_2 are enhanced considerably when the halogen-containing species are co-adsorbed with polar molecules (H_2O, NH_3, CH_3OH) [21, 27, 29, 30]. Figure 4 shows the variation in Cl^- and F^- ESD intensities for various coverages of CF_2Cl_2 on Ru(0001) as a function of H_2O overlayer coverage [30]. Strikingly, it is seen that for the lowest CF_2Cl_2 coverages both F^- and Cl^- yields increase greatly with the initial H_2O deposition, exhibit a maximum at $\leq$1 ML of H_2O, and then decrease with increasing H_2O coverage. The maximum Cl^- enhancement is up to two orders of magnitude: the anionic yield is enhanced by $\sim$100 times when $\approx$1 ML water ice is present. For identical CF_2Cl_2 pre-coverages, the maximum enhancement of Cl^- is much stronger than that of F^- [30]. The observed decrease in F^- and Cl^- with high H_2O coverage is expected because of elastic and inelastic scattering as the desorbed ions pass through the overlayer [21].

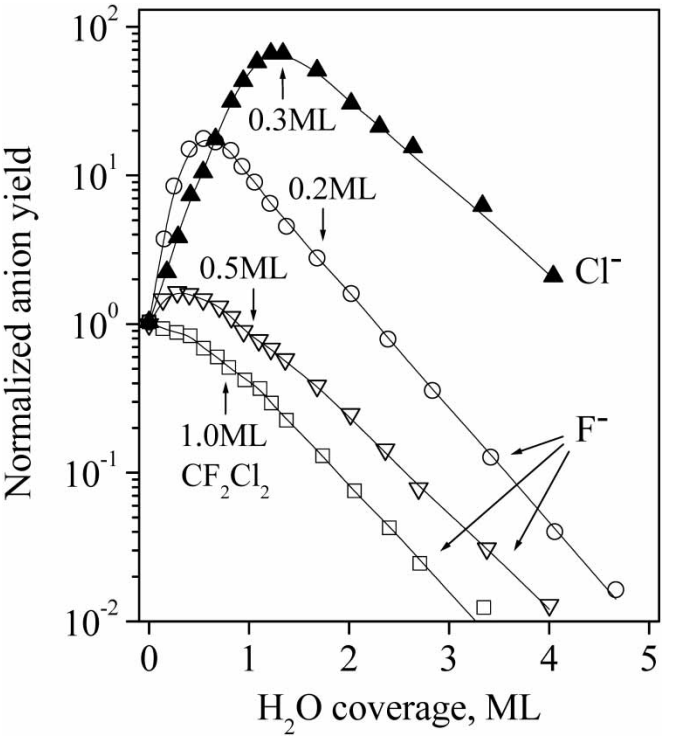

Figure 4. F^- and Cl^- ESD yields from CF_2Cl_2-precovered Ru(0001) as a function of H_2O overlayer thickness. Incident electron energy is 250 eV. Each data point represents the integrated intensity of the corresponding ESDIAD pattern. All data are obtained from ESDIAD measurements and calculated yields are normalized to the anion signal at zero water coverage (1 ML H_2O is associated with the formation of a hydrogen-bonded bilayer on ruthenium).

Downloaded At: 16:25 21 January 2011

To summarize, the data indicate a substantial enhancement of relative anionic ESD yield for fractional monolayers of CF_2Cl_2 on a metal surface upon co-adsorption with H_2O (results for co-adsorption with NH_3 and CH_3OH can be found elsewhere [14, 30, 89]).

4.3. *Thermal desorption of CF_2Cl_2 from the surface and bulk of water (ice)*

TPD is a straightforward but powerful technique for the study of halocarbons in condensed phases [27, 37, 90–94]. Such measurements can provide information about the interaction of molecules co-adsorbed at low temperature on metal surfaces, including the structure of halocarbon/water films (amorphous or polycrystalline) and the existence or absence of segregation. In principle, thermal reactions may occur between molecular or ionic fragments in the irradiated film during the substrate heating that accompanies TPD. However, our studies show clearly that no reactions between halocarbons and water are observed in the absence of prior irradiation by electrons or X-rays. Moreover, fragments such as COF_2, $COCl_2$ and C_2Cl_4 are seen in both TPD and RAIRS or XPS. The latter two indicate that these products are already formed at $\leq$100 K. Alternatively, such fragments as hydrated Cl^- ions or hydronium ions seen using RAIRS or XPS are clearly not seen in TPD.

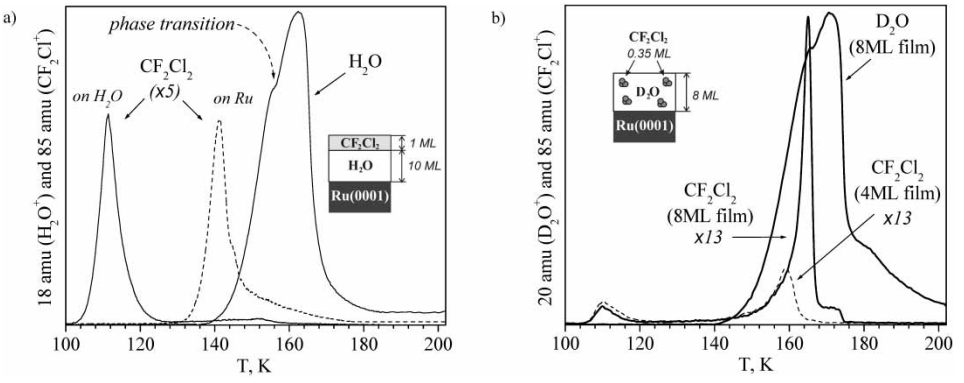

Figure 5. Thermal desorption spectra for CF_2Cl_2 co-adsorbed with water on Ru(0001) at 25 K. The spectra were measured at a heating rate of $\sim$1 K s^{-1}. (a) 1 ML of CF_2Cl_2 on top of $\sim$10 ML of H_2O (solid line); the dashed line is the spectrum for 1 ML of CF_2Cl_2 on a clean ruthenium surface. (b) Dilute ($\sim$4%) mixture of CF_2Cl_2 and D_2O with total film thickness $\sim$8 ML where the dashed line is the desorption spectrum for a thinner ($\sim$4 ML) CF_2Cl_2/ H_2O film. The data are reproduced from ref. [37].

Downloaded At: 16:25 21 January 2011

Figure 5(a) shows TPD spectra obtained for 1 ML CF_2Cl_2 on top of 10 ML water ice. The maximum desorption rate of H_2O is observed at $\approx$160 K. The H_2O spectrum also exhibits a distinct feature at $\sim$155 K, which is attributed to an irreversible structural transition from amorphous solid ice to a crystalline phase [95]. This spectrum is indistinguishable from that measured for water on Ru(0001) without the Freon overlayer [36]. CF_2Cl_2 starts to desorb from the solid water film long before the onset of H_2O desorption, reaching its maximum desorption rate at $\sim$110 K (see solid line for CF_2Cl_2 in figure 5(a)). This temperature is lower than the peak temperature ($\sim$140 K) for desorption of CF_2Cl_2 molecules in direct contact with the Ru crystal (shown by a dashed line), and nearly coincides with the temperature of multilayer Freon desorption [27].

Figure 5(b) illustrates thermal desorption spectra observed for CF_2Cl_2 molecules inside a D_2O matrix, following co-deposition of CF_2Cl_2 and D_2O. The solid line shows the spectrum for a dilute mixture consisting of 0.35 ML CF_2Cl_2 and 8 ML D_2O (corresponding concentration is $\sim$4%). The dashed line indicates the CF_2Cl_2 spectrum for a thinner film ($\sim$4 ML) of the same concentration. Both Freon spectra exhibit two distinct low- and high-temperature peaks, at $\sim$110 and $\sim$165 K ($\sim$160 K for 4 ML film), and a small shoulder at higher temperatures.

Comparison of the spectra shown in figures 5(a) and 5(b) suggest that the low-temperature peak ($\sim$110 K) in figure 5(b) corresponds to desorption of molecules from the ice surface. In the CF_2Cl_2 desorption curve the dominant high-temperature peak at $\sim$165 K correlates with the phase transition from amorphous to crystalline ice, which for D_2O occurs at $\sim$165 K [95]. This CF_2Cl_2 peak exhibits a smooth leading edge until the water crystallizes (figure 5(b)), followed by an abrupt drop and shoulder as the temperature increases further. Thus, the high-temperature CF_2Cl_2 desorption peak is attributed to the escape of CF_2Cl_2 molecules trapped in the bulk of the ice matrix; diffusion of Freon occurs through defects (cracks, fissures, grain boundaries, etc.) during the amorphous-to-crystalline-phase transition in the ice matrix followed by desorption (see discussion of 'molecular volcano' desorption in section 5.2).

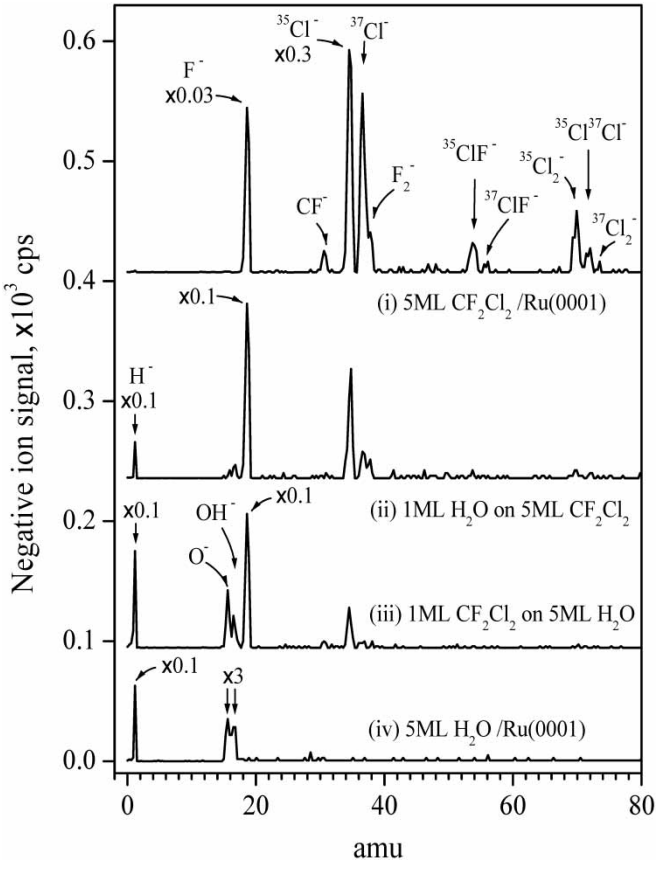

Figure 6. ESD mass spectra of negative ions obtained under electron irradiation (300 eV; exposure $\sim 5 \times 10^{14}\,\mathrm{cm}^{-2}$) of (i) 5 ML CF_2Cl_2 adsorbed on Ru(0001) at 25 K, (ii) 1 ML H_2O on 5 ML CF_2Cl_2, (iii) 1 ML CF_2Cl_2 on 5 ML H_2O, and (iv) 5 ML H_2O. The peaks marked by arrows and symbols $\times N$ are multiplied by factor N for clarity.

4.4. *Electron-stimulated desorption from halocarbon/water films: neutrals and negative ions*

Electron bombardment causes desorption of both neutral and ionic fragments from the surface of halocarbon/water films. Analysis of ionic/molecular ESD mass spectra provides important information about the interaction of electrons with adsorbed monolayers and condensed films.

Figure 6 shows a comparison of the gas-phase negative ions produced during electron irradiation of neat CF_2Cl_2 and CF_2Cl_2 co-adsorbed with water. The spectra measured for films containing Freon (top three spectra) show strong F^- ion signals, indicating that electron-induced desorption of the relatively low mass F^- ion from CF_2Cl_2 dominates [70]. The Cl^- fragment is the second most abundant ion fraction for thick ($\geq$ several ML) Freon films (see spectra (i) and (ii) in figure 6 for 5 ML CF_2Cl_2 and also corresponding figures in ref. [70] for higher coverage). For a thick film (5 ML) of neat CF_2Cl_2, CF^-, F_2^-, ClF^- and Cl_2^- ions are also observed. In addition to the anions observed for neat CF_2Cl_2 layers, co-adsorption of CF_2Cl_2 with water in figure 6 leads to the desorption of additional anions, notably

Downloaded At: 16:25 21 January 2011

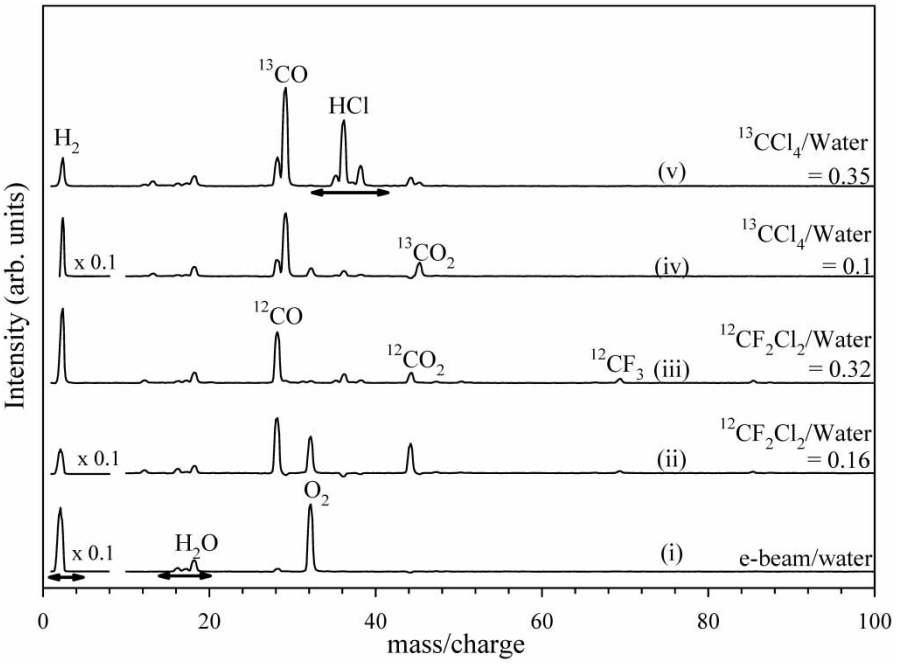

Figure 7. ESD mass spectra of neutral species detected under electron irradiation (200 eV, note higher electron exposure $\sim 1.5 \times 10^{16}\,cm^{-2}$ than in figure 6): (i) neat water, (ii) and (iii) $^{12}CF_2Cl_2$/water, and (iv) and (v) $^{13}CCl_4$/water and films. The spectra have been background subtracted to compensate for volatile neutral species present in the vacuum chamber.

Downloaded At: 16:25 21 January 2011

H^-, O^- and OH^- ions (see spectra (ii) and (iii) in figure 6), associated with the electron-stimulated dissociation of H_2O.

Figure 7 shows the variation in neutral volatile gas-phase products during electron-beam irradiation of CF_2Cl_2/water and CCl_4/water films at ~100 K. Typical total electron exposure during these experiments is considerably higher ($\sim 10^{16}\,cm^{-2}$ vs. $5 \times 10^{14}\,cm^{-2}$) than that used for figure 6. Representative dilute and concentrated films are shown for each organohalide. The evolution of neutral gas-phase products from electron-beam irradiation of water (ice) films is shown in figure 7(i), where the dominant neutral fragments are H_2 ($m/q = 2$) and O_2 ($m/q = 32$). Figures 7(ii)–(iii) and 7(iv)–(v) show the effect of the initial organohalide: water ratio upon the distribution of gas-phase products. This concentration effect is highlighted for CF_2Cl_2/water films by the increase in the $CO : CO_2$ ratio for concentrated films (figures 7(ii) and 7(iii)). Similarly, the production of molecular O_2 is suppressed in the presence of CF_2Cl_2 or CCl_4, becoming more pronounced for more concentrated films. Using isotopically labelled $^{13}CCl_4$ (figures 7(iv) and 7(v)), $^{13}CO/^{13}CO_2$ rather than $^{12}CO/^{12}CO_2$ are the dominant signals detected from the film proving that the CO/CO_2 fragments originate from the film rather than from the background.

To summarize, the negative ion fragment patterns (figure 6) indicate only features that are associated with unreacted parent molecules (CF_2Cl_2, H_2O) in the film. By contrast, the mass spectra of neutrals reveal strong evidence of reaction products, that is fragments corresponding to the production of other molecular species (e.g. H_2, CO, CO_2, O_2, HCl) as a result of electron-induced

decomposition of parent molecules and the subsequent reactions involving these fragments.

4.5. *Identification of electron-stimulated reaction products in halocarbon/water (ice) films*

4.5.1. *TPD studies*

TPD is an effective tool for identifying the decomposition products after electron irradiation. This information can be used to derive semiquantitative information on the reaction dynamics caused by electron bombardment. Comparative TPD spectra measured before and after electron irradiation (180 eV) of 0.2 ML CF_2Cl_2 adsorbed onto 5 ML D_2O are shown in figures 8(a) and 8(b), and corresponding spectra for 0.2 ML CCl_4 are shown in figures 8(c) and 8(d). Comparison of TPD spectra for a CF_2Cl_2/H_2O film before and after electron irradiation reveals that there is a notable decrease in the Freon signal (measured for mass 85, corresponding to CF_2Cl^+, the major fragment in the Freon cracking pattern) following exposure to $\sim 1 \times 10^{15}$ electrons cm^{-2} (figure 8(a)). Freon desorption temperatures before and after irradiation remain unchanged (~110 K).

Figure 8 illustrates how TPD can be used to detect parent and product signals from organohalide/H_2O (ice) films. Figures 8(a) and 8(b) show a comparison of the TPD signals associated with CF_2Cl_2 ($m/q = 85$; CF_2Cl^+) and COF_2 ($m/q = 47$; COF^+/CCl^+) before and after electron-beam irradiation. In contrast to the decrease in the CF_2Cl^+ signal, the intensity of the mass 47 signal (containing CCl^+, a minor fragment of Freon) increases after irradiation (figure 8(b)). In conjunction with RAIRS measurements, we assign this increase to a contribution from the COF^+ fragment (also mass 47), the major fragment of COF_2 (carbonyl difluoride) [96]. We also observe a much smaller than expected decrease in the $CFCl^+$ signal (mass 66 fragment of Freon; not shown in figure 8) due to a contribution from $COF_2{}^+$ (mass 66), the parent fragment of COF_2. Neither C_2F_4 (mass 100 $C_2F_4{}^+$ fragment) nor C_2F_6 (mass 119 $C_2F_5{}^+$ fragment) is observed in the TPD spectra after electron irradiation.

For 0.2 ML CCl_4 adsorbed on a D_2O ice surface, the post-irradiated TPD signal (figure 8(c); $m/q = 117$; $CCl_3{}^+$) for CCl_4 decreases even more rapidly than that observed for Freon for a similar electron-beam exposure. Desorption of several new species such as $COCl_2$ ($m/q = 63$; $COCl^+$) and C_2Cl_4 ($m/q = 164$; $C_2Cl_4{}^+$) are also detected. Formation of C_2Cl_6 during electron-beam irradiation of CCl_4/H_2O is ruled out, because we detect no signal for one of the expected fragments of C_2Cl_6 [94, 96], $C_2Cl_5{}^+$ (mass 199, not shown in figure 8).

In summary, the data in figure 8 indicate that electron bombardment of both halocarbons adsorbed on an ice layer induces their decomposition and chemical reactions in the condensed film. These reactions occur prior to heating the irradiated film (during TPD), as indicated by data presented below.

4.5.2. *RAIRS studies*

4.5.2.1. Product identification during irradiation of CF_2Cl_2/water films

Whereas TPD requires us to destroy the condensed halocarbon/water film in order to detect reaction products, the use of RAIRS allows us to detect reactants and products *in situ*. Figures 9 and 10 illustrate the molecular products observed by

Downloaded At: 16:25 21 January 2011

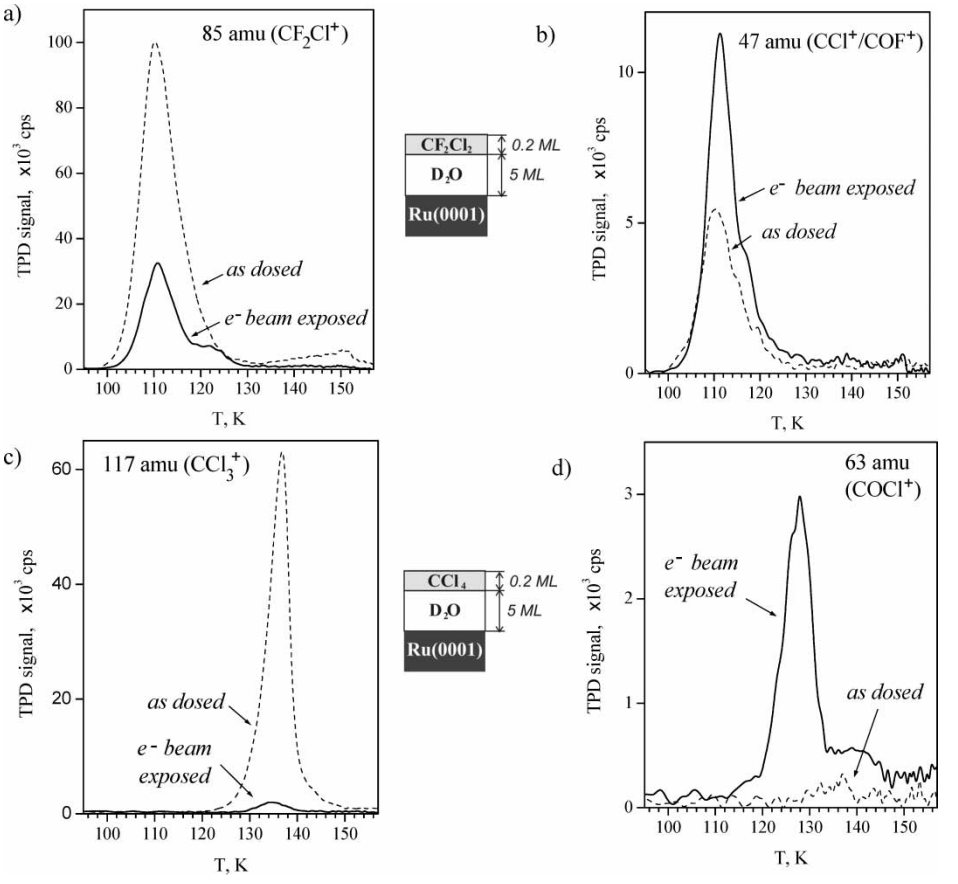

Figure 8. Thermal desorption spectra measured at heating rate $\sim 2\,K\,s^{-1}$ before (dashed lines) and after 180 eV electron irradiation (solid lines) of 0.2 ML halocarbon ((a, b) CF_2Cl_2; (c, d) CCl_4) adsorbed on top of 5 ML D_2O ice at 25 K. For 'electron-beam exposed' spectra the total electron exposure was $\sim 1 \times 10^{15}\,cm^{-2}$. Shown are fragments CF_2Cl^+ (85 mu) and CCl^+/COF^+ (47 mu) for CF_2Cl_2/D_2O, and CCl_3^+ (117 amu) and $COCl^+$ (63 amu) for CCl_4/D_2O. The spectra demonstrate decomposition of CF_2Cl_2 and CCl_4 (a,c) and production of COF_2 (b) and $COCl_2$ (d) under electron bombardment of the adsorbed layer. The data are reproduced from ref. [37].

RAIRS when thick CF_2Cl_2/water (ice) films ($\sim$30 nm) adsorbed on polycrystalline Au at 100 K are exposed to X-ray or electron-beam irradiation. Figures 9(ii) and 9(iii) show the effects of X-ray irradiation on a CF_2Cl_2/water (CF_2Cl_2: $H_2O \approx 0.28$) film, while figure 9(iv) shows the effects of electron irradiation on a different CF_2Cl_2/water ($CF_2Cl_2 : H_2O(0.2)$ film. The initial spectrum detected after adsorption (marked 'as deposited') exhibits IR bands associated with H_2O and CF_2Cl_2 (see table 1 for assignments). Irradiation of the film results in the appearance of new peaks assigned to CO_2 and COF_2. No evidence for bands associated with the production of carbonyl chloride fluoride (COFCl) or phosgene ($COCl_2$) is observed [97, 98]. The broad absorption feature centred at $\sim 1700\,cm^{-1}$ is consistent with the formation of hydronium ions [99], while the broadening and red shifting of the ν(O–H) stretching mode is also consistent with previous studies on the effect of

Downloaded At: 16:25 21 January 2011

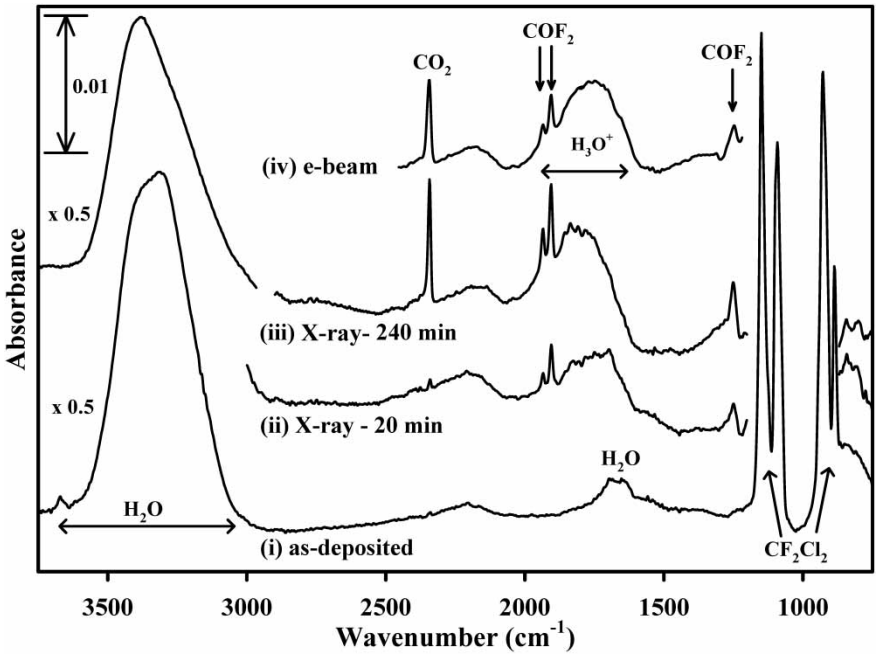

Figure 9. RAIR spectra of a CF_2Cl_2/H_2O ($CF_2Cl_2 : H_2O(0.28)$ film showing the effect of X-ray exposure: (i) as deposited, (ii) 20 min, (iii) 240 min and (iv) after 5 min electron irradiation ($CF_2Cl_2 : H_2O(0.2)$. All RAIR spectra were referenced to the clean cooled Au substrate. Peak assignments are given in table 1. After ref. [36].

Downloaded At: 16:25 21 January 2011

H_3O^+ production in ice films [73, 100]. It should be noted that no evidence of H_3O^+ production is observed during electron-beam or X-ray irradiation of pure water ice films, indicating that these species form as a result of reactions involving CF_2Cl_2 and/or its decomposition products [38]. An inspection of additional peaks after electron-beam irradiation in figure 9(iv) indicates that the molecular products are the same as those produced by X-ray irradiation, namely, the production of COF_2, CO_2 and H_3O^+ species (table 1).

Figure 10 illustrates the variation in the integrated IR intensities of the CF_2Cl_2, COF_2 and CO_2 product peaks during (a) X-ray ($CF_2Cl_2 : H_2O \sim 0.1$) and (b) electron irradiation ($CF_2Cl_2 : H_2O(0.2)$ of CF_2Cl_2/H_2O films. The data are measured for thick ($\sim$30 nm) films adsorbed on polycrystalline Au at 100 K. In the case of X-ray irradiation, changes in the RAIR spectra are dominated initially (<50 min) by the decrease in the CF_2Cl_2 area accompanied by the appearance of COF_2. The dashed line in figure 10(a) is a best-fit first-order decay profile for the loss of CF_2Cl_2 from the film, which incorporates the non-uniform spatial intensity profile anticipated for the X-ray source [101]. For CO_2 production, however, there is a short induction period at low X-ray exposures (<40 min) before a roughly linear increase for longer X-ray irradiation times. Figure 10(a) also shows that the area of the COF_2 peak passes through a maximum and decreases upon prolonged X-ray exposure (>180 min).

Figure 10(b) shows the corresponding IR intensity variation of the carbon-containing fragments as a function of electron-beam irradiation. A comparison of figures 10(a) and 10(b) indicates that although the qualitative variations in the IR

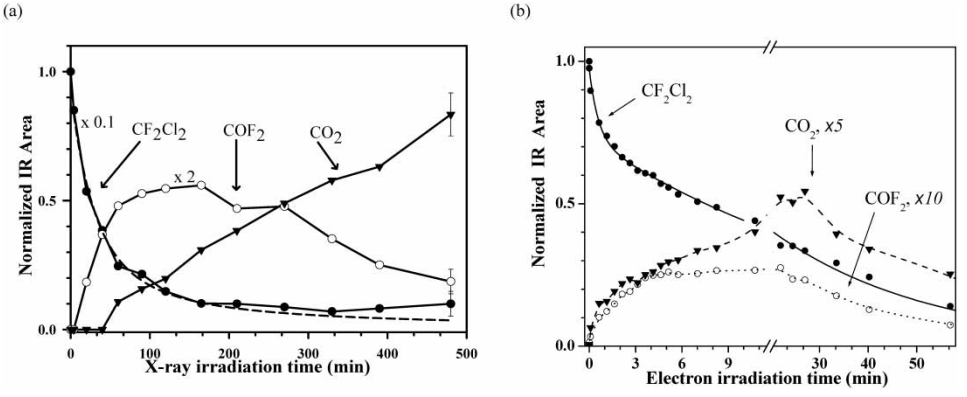

Figure 10. Variation in the IR integrated intensities of the parent (1146 and 1090 cm^{-1}) and carbon-containing products COF_2 (1936 and 1906 cm^{-1}) and CO_2 (2339 cm^{-1}) bands as a function of (a) X-ray and (b) electron-beam irradiation, where the solid and dashed lines in (b) are a guide to the eye. The dashed line in (a) represents the best-fit first-order decay calculated for the loss of CF_2Cl_2, which incorporates the non-uniform spatial intensity profile of the X-ray beam. After refs [36] and [37].

Downloaded At: 16:25 21 January 2011

Table 1. Observed frequencies in the infrared spectrum of CF_2Cl_2/H_2O ice films[a]

Frequencies (cm^{-1})	Assignment	Mode description
3000–3600	H_2O	ν(O–H) str.
2339	$^{12}CO_2$	$\nu(^{12}C{=}O)$ str.
1936	COF_2	ν_1(CO) str.
1906	COF_2	$2\nu_2$(C–F) str. (FR)
1560–1950	H_3O^+	$\delta_a(H_3O^+)$ def.
1600–1700	H_2O	$\delta(H_2O)$ def.
1180–1250	H_3O^+	$\delta_s(H_3O^+)$ def.
1248	COF_2	ν_4(C–F) str.
1146	CF_2Cl_2	ν_{as}(C–F) str.
1090	CF_2Cl_2	ν_s(C–F) str.
928	CF_2Cl_2	ν_{as}(C–Cl) str.
886	CF_2Cl_2	δ(C–F) + γ(C–F) (FR)

FR, Fermi resonance; γ, out-of-plane deformation; ν_s, symmetric stretch; δ, in-plane deformation; ν_{as}, asymmetric, stretch. [a]Ref. [98].

intensities of CF_2Cl_2, COF_2 and CO_2 species are similar, the fate of the final decomposition product CO_2 depends upon the primary irradiation source. In the case of X-rays, CO_2 is stable within the film [36]. By contrast, CO_2 is both produced and lost from the film as a result of electron-stimulated reactions, evidenced by the variation in the RAIR spectra shown in figure 10(b).

4.5.2.2. Product identification during irradiation of $CDCl_3$/water films

For comparison with CF_2Cl_2 and CCl_4 we show RAIRS data for $CDCl_3$ in figure 11. The RAIRS data reveal a range of decomposition products including CO_2, $COCl_2$ and H_3O^+. The initial spectrum is referenced to the Au substrate, while the

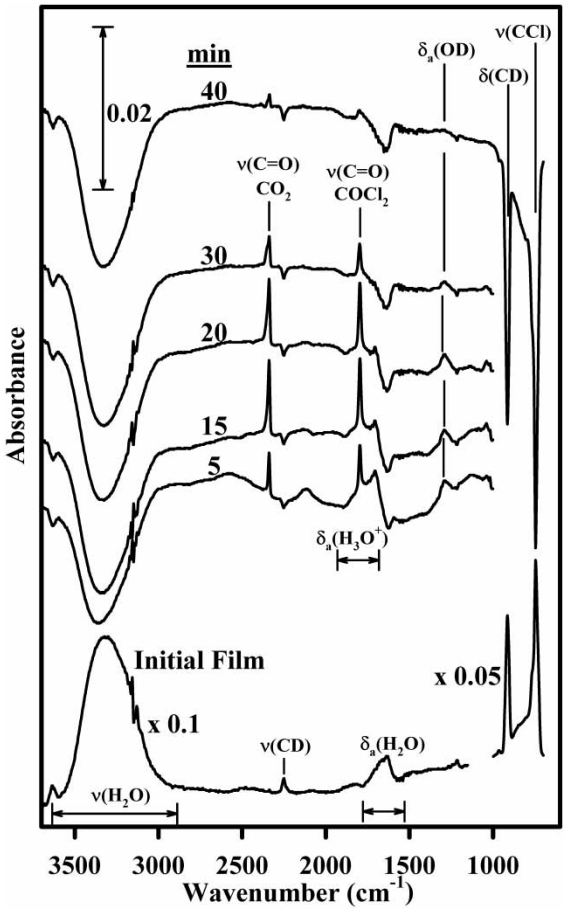

Figure 11. RAIR spectra of $CDCl_3/H_2O$ film as a function of electron-beam irradiation ($CDCl_3 : H_2O(0.24)$ (estimated exposure per minute $\sim 4 \times 10^{16}\,cm^{-2}$). The spectra as a function of electron exposure are referenced to the initial organohalide film. Negative peaks indicate the loss of the parent molecules.

subsequent spectra are referenced to the initial film. Referencing each spectrum to the initial film enables us to clearly distinguish peaks that are due to products (positive peaks) and to the loss of parent $CDCl_3$ (negative peaks) in electron-stimulated reactions.

In the initial film, bands at 2252, 914 and 746 cm^{-1} are assigned to C–D stretch, in-plane C–D bending and C–Cl stretching modes of $CDCl_3$, respectively. Upon electron-beam irradiation, additional bands are observed at 2339 and 1798 cm^{-1}, which are assigned to $COCl_2$ and CO_2, respectively (table 2). Features centred at $\sim$1700 and $\sim$1290 cm^{-1} are detected and attributed to O–H and O–D in-plane bending modes of H_3O^+ and $H_xD_{3-x}O^+$, respectively. The CO_2, $COCl_2$, H_3O^+ and $H_xD_{3-x}O^+$ intensities grow to maxima and then decrease upon prolonged electron irradiation. This growth and decrease of the carbon-containing products $COCl_2$ and CO_2 upon electron irradiation is qualitatively similar to that seen for CCl_4/water films [39]. Negative absorption peaks observed between 3600–3000 and 920–730 cm^{-1} are due to the electron-stimulated consumption of both H_2O and $CDCl_3$.

Downloaded At: 16:25 21 January 2011

Table 2. IR assignments of parent and product peaks observed in electron-stimulated reactions of chlorocarbon/water (ice) films[a]

Frequencies (cm^{-1})	Assignment	Mode description
2339	$^{12}CO_2$	$\nu(^{12}C{=}O)$ str.
2272	$^{13}CO_2$	$\nu(^{13}C{=}O)$ str.
1936	$^{12}COF_2$	ν_1(CO) str.
1906	$^{12}COF_2$	$2\nu_2$(C–F) str. (FR)
1950–1560	H_3O^+	$\delta_a(H_3O^+)$ def.
1798	$^{12}COCl_2$	$\nu(^{12}C{=}O)$ str.
1750	$^{13}COCl_2$	$\nu(^{13}C{=}O)$ str.
1426	$^{12}CH_3I$	$\delta_s(CH_3)$ def.
1430–1390	Hydronium ion	δ(OD) def.
1400	$^{12}CH_3I$	$[\nu(C–I)+\rho(CH_3)]$ (FR)
1300	$^{12}CH_4$	(CH_3) def.
1290	Hydronium ion	δ(OD) def.
1248	$^{12}COF_2$	ν_4(C–F) str.
960	$^{12}CD_2Cl_2$	CD wag
916	$^{12}CDCl_3$	$\delta(^{12}C–D)$ def
914	$^{12}C_2Cl_4$	$\nu(^{12}C–Cl_2)$ str.
890	$^{12}CH_3I$	$\rho(CH_3)$ rock
885	$^{13}C_2Cl_4$	$\nu(^{13}C–Cl_2)$ str.
855	$^{12}COCl_2$	$\nu(^{12}C–Cl_2)$ str.
825	$^{13}COCl_2$	$\nu(^{13}C–Cl_2)$ str.

[a]Refs [97, 98].

Downloaded At: 16:25 21 January 2011

It should be noted that the intensity of the IR peaks associated with the various product species scale with the film thickness, indicating that reaction products originate within the film rather than at the Au/film interface.

4.5.2.3. Influence of halocarbon speciation on reaction products probed by RAIRS

Infrared spectroscopy enables us to identify the reaction products from their 'fingerprint' vibrational frequencies. Figure 12 summarizes the new vibrational features observed during X-ray or electron irradiation of the different halocarbons (CF_2Cl_2, CCl_4, $CDCl_3$, CD_2Cl_2, CH_3I) each having organohalide : water ratios in the range 0.2–0.35. All RAIR spectra are referenced to the signals from their initial films in order to delineate between decomposition products (positive) and parent halocarbon/water bands (negative). Figure 12(i)–(iii) shows the observed electron-stimulated decomposition products of the Freon/water (ice) and CCl_4/water (ice) films. A comparison of the region above 2200 cm^{-1} in figure 12(i)–(iii) for CF_2Cl_2/water and CCl_4/water films indicates that the carbon-containing products are CO_2 and COF_2 (for CF_2Cl_2) and $COCl_2$ (for CCl_4) along with hydrated hydronium ions (table 2). Figure 12(ii)–(iii) shows the effect of electron bombardment upon $^{12/13}CCl_4/H_2O$ films. Inspection of the wavenumber region below 1500 cm^{-1} also enables us to identify additional bands due to the C–Cl stretching modes of phosgene $COCl_2$ (^{12}C–Cl; 855 cm^{-1} and ^{13}C–Cl; 825 cm^{-1}) and for CCl_4/H_2O films the C–Cl stretching modes associated with tetrachloroethene C_2Cl_4 (^{12}C–Cl; 914 cm^{-1} and ^{13}C–Cl; 885 cm^{-1}) [38, 39].

Figure 12(ii), (iv)–(vi) illustrates the effect of irradiation on a series of halocarbon films with decreasing halogen content: CCl_4, $CDCl_3$, CD_2Cl_2 and CH_3I.

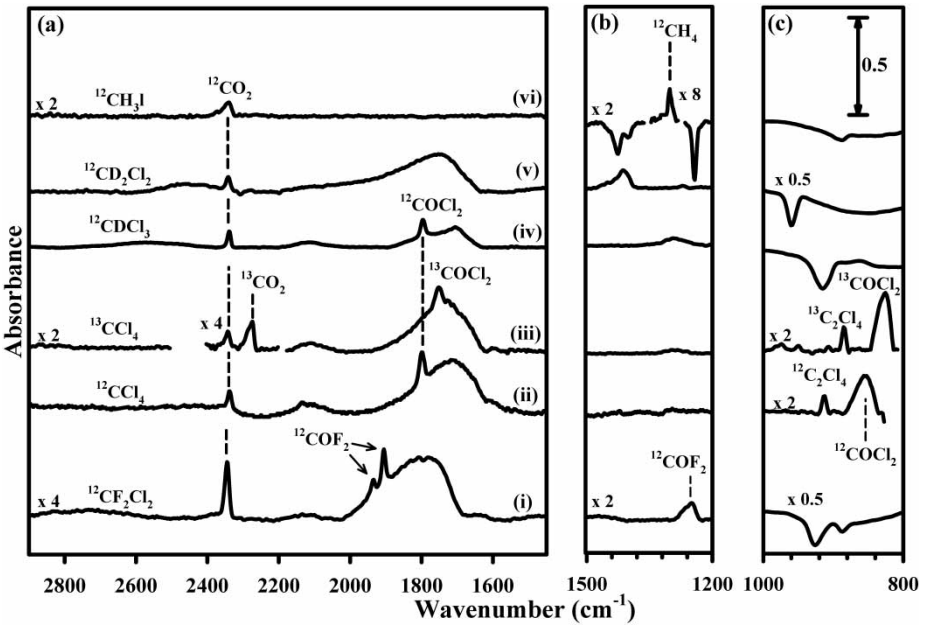

Figure 12. RAIR spectra of (i) $^{12}CF_2Cl_2$, (ii) $^{12}CCl_4$, (iii) $^{13}CCl_4$, (iv) $^{12}CDCl_3$, (v) $^{12}CD_2Cl_2$ and (vi) $^{12}CH_3I$ water films illustrating the carbon-containing reaction products within the film after electron-beam exposure. Negative peaks are due to parent loss. Wavenumber ranges are: (a) 2900–1450 cm^{-1}; (b) 1500–1200 cm^{-1} and (c) 1000–800 cm^{-1}. All spectra were normalized to the $^{12}CO_2$ peak area and were referenced to their initial halocarbon films prior to electron exposure. Peak assignments are given in table 2.

Downloaded At: 16:25 21 January 2011

$CDCl_3$/water films, in common with CCl_4/water films, have bands assigned to the ν(C=O) stretching modes of CO_2 and $COCl_2$ at 2339 and 1798 cm^{-1}, respectively (table 2). Similarly, there are broad bands associated with the in-plane bending modes of protonated and deuterated hydronium ions centred at ~1700 and ~1290 cm^{-1}, respectively (table 2). CD_2Cl_2/water films, in contrast to CCl_4/water and $CDCl_3$/water films, have no phosgene ($COCl_2$) peaks. Upon electron-beam irradiation of methyl iodide (CH_3I), bands at 2339 and 1300 cm^{-1} are observed, which can be assigned to CO_2 and methane (CH_4), respectively (see table 2 for assignments).

A comparison of figures 12(i) and 12(vi) reveals the following trends: CO_2 is produced in all of the films, while the formation of hydronium ions and the intermediate species COX_2 (X=Cl, F) is dependent upon the chemical identity of the organohalide. Hydronium ions are produced during electron-stimulated reactions with CX_4 (CF_2Cl_2, CCl_4), CHX_3 (e.g. $CDCl_3$) and CH_2X_2 (e.g. CD_2Cl_2) species adsorbed on ice films. Carbonyl dihalide (COX_2) species, however, are only formed during electron-stimulated decomposition of the CX_4 and CHX_3 species. CH_3I, by contrast, does not produce carbonyl dihalides or hydronium ions.

4.5.3. *Evolution of halocarbon/water (ice) film during electron-stimulated reactions: production of halide anions*

XPS brings additional insights that are not accessible by RAIRS or TPD. Thus, although RAIRS can often provide unambiguous identification of reaction products,

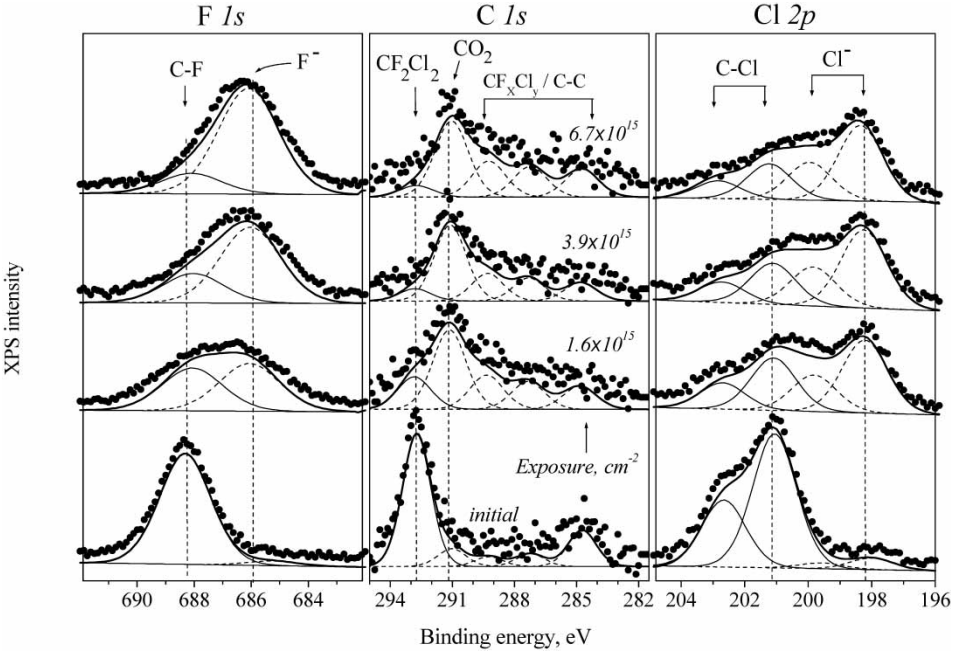

Figure 13. Transformation of (a) F 1s, (b) C 1s and (c) Cl 2p XPS regions of CF_2Cl_2 in H_2O matrix as a function of electron exposure (labelled in C 1s plot). A film with halocarbon/water ratio ~0.06 and thickness ~6.5 nm was deposited on a Au substrate at ~100 K. Incident electron energy is 210 eV. Spectra for C 1s region are presented with the background subtracted. The data are reproduced from ref. [37].

Downloaded At: 16:25 21 January 2011

the ability to identify a specific reaction product is sometimes limited by the concentration and relative oscillator strength of chromophores within the product molecule. By contrast, XPS can provide quantitative information on the chemical composition of surfaces and thin films and can also often identify different chemical states for specific elements based on binding energies. In particular, XPS allows identification of such species as solvated ions (Cl^-, F^-) that cannot be directly identified using the other two techniques. Thus, Figure 13 shows the evolution of the F 1s, C 1s and Cl 2p XPS data for a CF_2Cl_2/H_2O film ($CF_2Cl_2 : H_2O \approx 0.06$) as a function of electron exposure. The XPS peaks associated with CF_2Cl_2 are the single C–F peak in the F 1s region (≈688 eV) and a C–Cl $2p_{3/2}/2p_{1/2}$ doublet in the Cl 2p region, with the $2p_{3/2}$ peak located at ≈201 eV [36]. In addition, the C 1s peak associated with the native CF_2Cl_2 species can be observed at ~293 eV [36], while the peak at 285 eV is assigned to adventitious carbon contamination.

During electron irradiation, changes are observed in the F 1s, Cl 2p and C 1s regions. At small electron exposures ($<10^{15}$ cm^{-2}), the Cl 2p XPS spectral envelope broadens to lower binding energies, consistent with the growth of a new $2p_{3/2}/2p_{1/2}$ doublet with a $2p_{3/2}$ peak at ≈198 eV indicative of the formation of chloride ions in the film [102]. For the corresponding electron exposure in the C 1s region, a new peak appears at ≈291 eV at the expense of the native CF_2Cl_2 peak. RAIRS data indicate that in dilute films where the $CF_2Cl_2 : H_2O$ ratio is low, CO_2 is expected to be the dominant carbon-containing molecular species in the film after prolonged electron exposures, enabling us to identify the peak at ≈291 eV as CO_2. This peak

position also coincides with results obtained during control experiments involving CO_2 deposition onto ice films. Although the production of chloride ions is dominant during the initial stages of irradiation, for longer electron exposures ($>10^{15}\,cm^{-2}$) the appearance of fluoride ions becomes increasingly apparent in the F 1s region; this is evidenced by the broadening of the F 1s region to lower binding energies, indicating the growth of a new peak centred at ~686 eV. Figure 13 also shows that, for prolonged electron exposures, the XPS peaks associated with chloride and fluoride ions in the Cl 2p and F 1s regions become the dominant features relative to C–Cl and C–F species.

4.6. *Effects of substrate temperature on the stability of carbon-containing species in irradiated CF_2Cl_2/water films*

All of the data presented up to this point have focused on processes that occur during electron bombardment at the adsorption temperature. Here we describe the use of XPS to probe the relative thermal stability of carbon-containing fragments produced from electron-stimulated decomposition of CF_2Cl_2/H_2O films. Figure 14 illustrates the effects of substrate annealing on a CF_2Cl_2-rich film ($CF_2Cl_2 : H_2O \approx 0.8$) following 230 min of X-ray irradiation. Figure 14(i) shows the initial C 1s region, containing only a single peak at ~292.5 eV assigned to CF_2Cl_2 species. After 230 min of X-ray irradiation, the C 1s region shows that most, if not all, of the CF_2Cl_2 has reacted. A new peak is evident at ~291 eV whose peak position is consistent with the presence of either CO_2 or COF_2 (or both) [36]; in addition, a broad C 1s spectral envelope develops at lower binding energy relative to the parent CF_2Cl_2 peak (figure 14(ii)). Following X-ray irradiation, this film was heated to increasingly higher substrate temperatures. Figure 14(iii) shows that upon annealing the surface to 220 K, a temperature at which CF_2Cl_2, H_2O, CO_2 and COF_2 species are expected to have desorbed based on TPD, the peak at 291 eV disappears while the broad C 1s envelope extending to lower binding energies remains. Above 220 K the C 1s XPS signal remains almost constant until the surface is heated above 500 K, when the broad C 1s peak profile is replaced by a dominant peak at 285 eV (compare figures 14(iv) and 14(v)) assigned to the formation of a graphitic overlayer. Corresponding measurements in the F 1s and Cl 2p regions indicate that changes in the C 1s region upon annealing to 500 K correlate with the desorption of C–Cl and C–F species, evidenced by the loss of C–Cl and C–F species from the Cl 2p and F 1s regions respectively (not shown). Based on these measurements, we conclude that the broad C 1s envelope observed in figure 14 is associated with a polymeric CF_xCl_y residue that is stable above room temperature.

4.7. *Effect of the film's initial chemical composition on product partitioning*

Another important issue is the effect of halocarbon concentration in a water (ice) matrix and how it influences the distribution of products formed by high-energy irradiation. Figures 15–17 illustrate the effect of the film's halocarbon : water ratio on the product distribution after fixed amounts of electron or X-ray exposure. In particular, we probe the fate of the carbon-containing fragments by RAIRS and XPS.

Figure 15 shows RAIR spectra illustrating the effect of the film's initial $CF_2Cl_2 : H_2O$ ratio on the distribution of COF_2 and CO_2 after a fixed period of X-ray exposure (40 min). In these experiments, the total amount of CF_2Cl_2 within the film was held constant on the basis of the integrated area of the parent IR peaks at 1146 and 1090 cm^{-1} while the relative amount of the H_2O (measured by the

Downloaded At: 16:25 21 January 2011

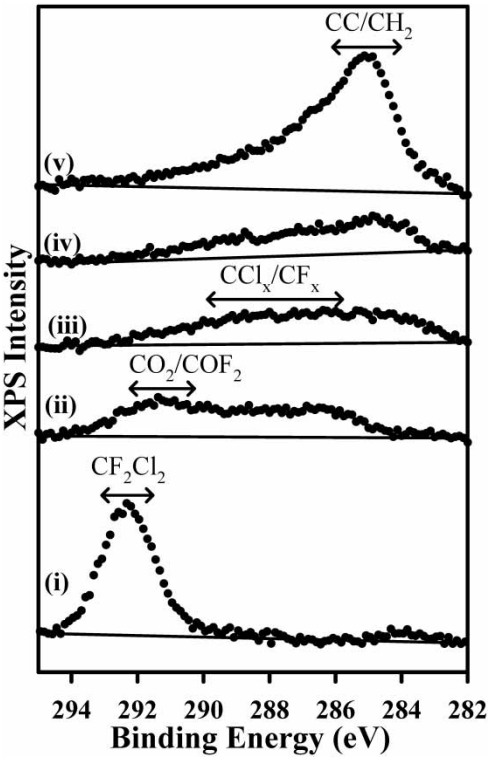

Figure 14. C 1s XPS showing the effect of annealing temperature on an X-ray irradiated CF_2Cl_2/H_2O layer (CF_2Cl_2: H_2O(0.8)): (i) for the initial film adsorbed at 100 K, (ii) after 230 min X-ray irradiation, and then after subsequent annealing to (iii) 220 K, (iv) 273 K and (v) 560 K. Spectra (iii)–(v) were taken above 200 K to minimize re-adsorption of background gases (CO_2, CF_2Cl_2, H_2O). After ref. [36].

Downloaded At: 16:25 21 January 2011

integrated area of the O–H stretching mode) was varied (see table 1 for assignments). Thus, the film thickness was varied in different experiments. This approach was used to ensure that the total amount of initial carbon-containing species (i.e. CF_2Cl_2) in the films was constant while the $CF_2Cl_2 : H_2O$ ratio was varied. Figure 15 shows that the concentration of CO_2 and COF_2 produced is dependent upon the film's initial CF_2Cl_2: H_2O ratio, being greatest for more H_2O-rich films.

Figures 16(a) and 16(b) shows the variation in the F 1s and Cl 2p XPS regions following 20 min of X-ray exposure for four films with different initial $CF_2Cl_2 : H_2O$ ratios. This is shown explicitly in figure 16(c) where the fraction of the total Cl and F signal composed of Cl^- and F^- anions after 20 min of X-ray irradiation is plotted as a function of the film's initial $CF_2Cl_2 : H_2O$ ratio. Figure 16(c) shows that the F^- and Cl^- anion production is sensitive to the film's initial chemical composition, with the greatest fraction of anions being produced in dilute films.

Figure 17 highlights the effect of initial chemical composition on the distribution of the carbon-containing fragments, using CD_2Cl_2/H_2O as an illustrative example. In figure 17, the C 1s XP spectra for CD_2Cl_2/H_2O films of different initial $CD_2Cl_2 : H_2O$ ratios were measured after the same electron exposure. The C 1s region prior to electron exposure consists of a single peak centred at 286.5 eV due to CD_2Cl_2 while

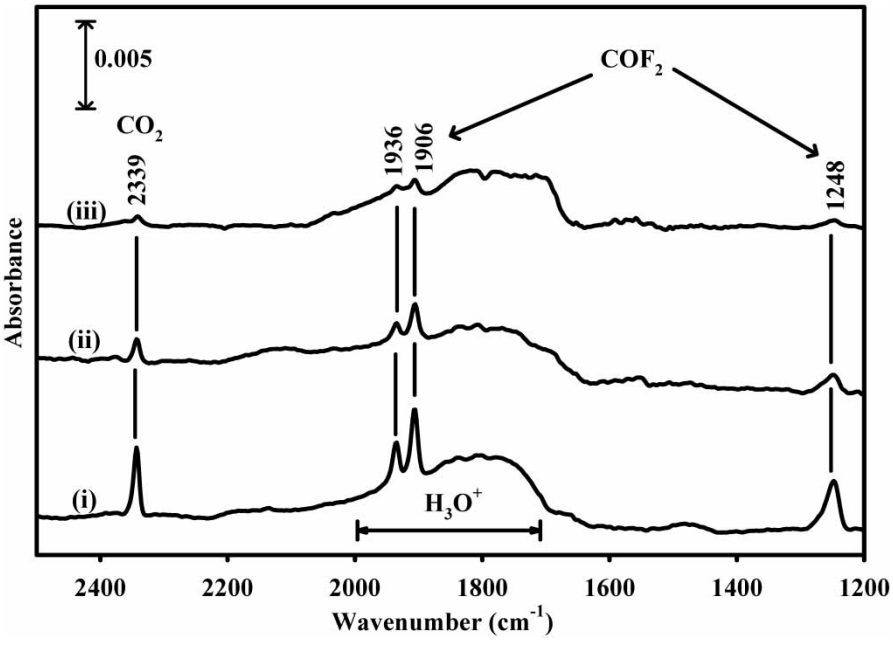

Figure 15. Variation in the IR spectra for (i) $CF_2Cl_2 : H_2O \approx 0.09$, (ii) $CF_2Cl_2 : H_2O \approx 0.19$ and (iii) $CF_2Cl_2 : H_2O \approx 0.26$ films after 40 min of X-ray irradiation. The spectra are difference spectra referenced to the initial CF_2Cl_2/H_2O film. Peak assignments are given in table 1.

Downloaded At: 16:25 21 January 2011

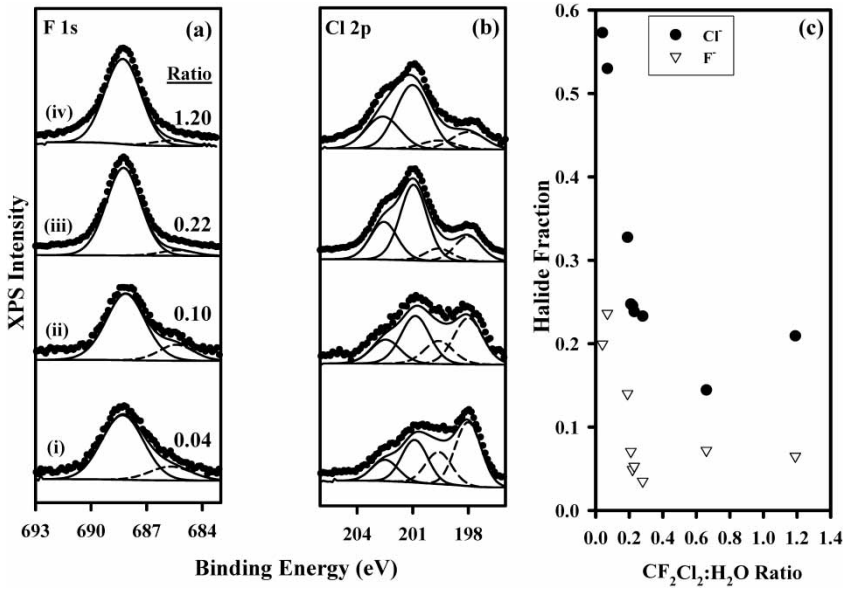

Figure 16. Variation in the (a) F 1s and (b) Cl 2p XPS regions for a series of different $CF_2Cl_2 : H_2O$ ratio ((i) 0.04, (ii) 0.1, (iii) 0.22, (iv) 1.20) films following 20 min of X-ray irradiation. The solid lines in the F 1s and Cl 2p regions correspond to the initial C–F and C–Cl species, while the dashed lines correspond to the F^- and Cl^- species. (c) Cl^-/Cl_{tot} and F^-/F_{tot} ratios following 20 min of X-ray irradiation as a function of the film's initial $CF_2Cl_2 : H_2O$ ratio. After ref. [36].

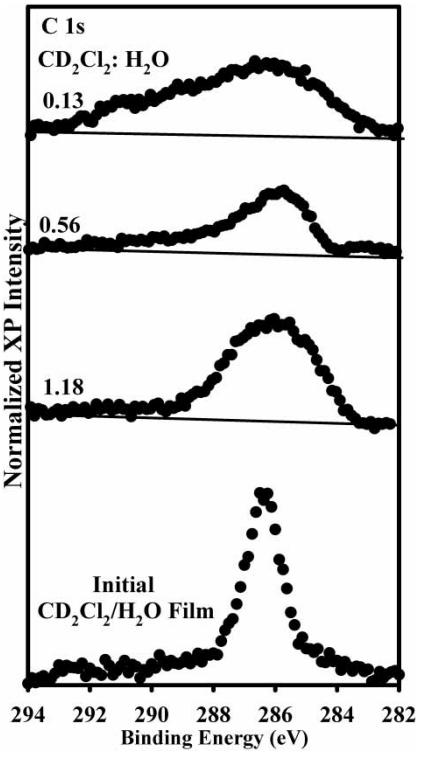

Figure 17. C 1s XP region of CD_2Cl_2/water films at ~100 K illustrating the effect of initial film composition on the product distribution. All spectra are normalized to the total C 1s area. Each spectrum corresponds to an individual CD_2Cl_2/water film that has been exposed to similar total electron exposures ($\sim 10^{17}$ cm^{-2}).

Downloaded At: 16:25 21 January 2011

the Cl 2p region (not shown) consists of a single Cl $2p_{3/2}/2p_{1/2}$ doublet. Upon electron-beam irradiation, the evolution of the C 1s spectral envelope is sensitive to the film's initial composition. In CD_2Cl_2-rich films, the spectral intensity is localized around the position of the parent peak. With increasing dilution, however, the distribution of intensity shifts to higher binding energy, with an additional peak at ~291 eV. XP intensity at ~291 eV was assigned to the production of CO_2 in dilute CCl_4/water films. In XPS, C 1s spectral features at lower binding energies (between 285 and 290 eV) were attributed to the formation of a partially halogenated (CCl_x) polymeric residue.

These results are consistent with previous electron-beam irradiation studies of CCl_4/water (ice) films, which show that the distribution of carbon-containing fragments is sensitive to the initial halocarbon : water (ice) ratio after a fixed period of irradiation time [38]. Thus, analysis of the C 1s region reveals that for a given period of electron-beam irradiation, the relative contribution from the partially chlorinated polymeric residue (CCl_x) is most pronounced in concentrated films where the initial $CD_2Cl_2 : H_2O$ ratio is highest. In addition, analysis of the data for CO_2 and $COCl_2$ yields in CCl_4/water (ice) films following a fixed period of electron-beam irradiation reveals that, except at high water dilutions where the amount of CCl_4 is low, the CO_2 and $COCl_2$ yields increase linearly with increasing initial $H_2O : CCl_4$ film ratios.

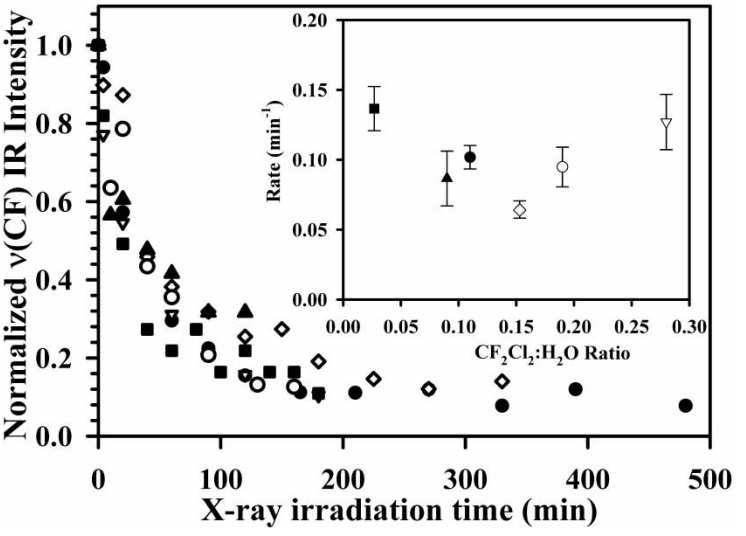

Figure 18. Plot of the ν(CF) band intensity for a series of CF_2Cl_2/H_2O films of different initial chemical composition as a function of X-ray irradiation time: $CF_2Cl_2:H_2O$= 0.03 (■), $CF_2Cl_2:H_2O$=0.09 (▲), $CF_2Cl_2:H_2O$=0.11 (●), $CF_2Cl_2:H_2O$=0.15 (◇), $CF_2Cl_2:H_2O$=0.19 (○) and $CF_2Cl_2:H_2O$=0.28 (▽). In each case, the amount of CF_2Cl_2 present in the film was determined from the integrated intensity of the ν(CF) bands (1090 and 1146 cm^{-1}) normalized to the initial ν(CF) integrated intensity. The insert shows the rate of CF_2Cl_2 loss calculated from a first-order fit that accounts for the non-uniform spatial profile of the X-ray source [36].

Downloaded At: 16:25 21 January 2011

4.8. *Electron-stimulated decomposition kinetics of CCl_4 and CF_2Cl_2*

Up to this point we have focused on the identification of the products in electron-stimulated reactions of halocarbon/water (ice) films. Now we address the kinetics and dynamics of the initial DEA process at both a qualitative and a semiquantitative level.

4.8.1. *RAIRS results: CF_2Cl_2*

In contrast to figures 15–17, which show the effect of the film's initial chemical composition on the concentrations of COF_2 and CO_2 after a fixed period of X-ray or electron irradiation, figure 18 illustrates the influence of the film's initial chemical composition on the kinetics of the parent CF_2Cl_2 loss. Figure 18 represents the loss of CF_2Cl_2 parent measured by the decrease in the integrated IR area of the ν(CF) bands as a function of X-ray irradiation for six films that possess different initial $CF_2Cl_2:H_2O$ ratios. Four of the films have an identical initial H_2O content (measured by the area of $\nu(OH)_{t=0}$) and two have a constant CF_2Cl_2 content ($\nu(CF)_{t=0}$)); consequently, the films prepared were of different thicknesses. Analysis of figure 18 reveals that the rate of CF_2Cl_2 loss calculated from the nonlinear regression of a first-order decay function is *not* strongly dependent upon the film's initial chemical composition as shown explicitly in the inset.

4.8.2. *TPD results: CCl_4 and CF_2Cl_2*

A comparison of the electron beam-induced decomposition of CCl_4 and CF_2Cl_2 is shown in figure 19. The semilogarithmic plots in figure 19 are the areas of

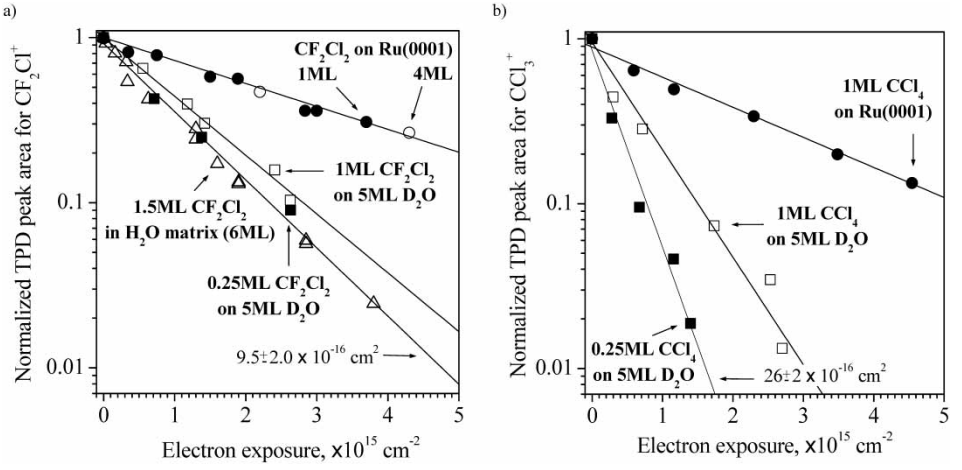

Figure 19. Dynamics of decomposition of halocarbons adsorbed on Ru(0001) and a thick (5 ML) D_2O film at 25 K, observed during irradiation by 180 eV electrons. Each point represents the integrated area of the TPD spectrum for either CF_2Cl_2 (a) or CCl_4 (b). Halocarbon thickness: 0.25 ML on D_2O (■), 1 ML on D_2O (□), and 1 ML on Ru (●). In (a) data were obtained (△) for a dilute mixture of CF_2Cl_2/H_2O (Freon: water ratio is 1 : 4) and (○) for 4 ML CF_2Cl_2 on Ru. The lines drawn through the data points are exponential fits (see text for details). The data are reproduced from ref. [41].

Downloaded At: 16:25 21 January 2011

corresponding TPD spectra versus electron exposure. The data are measured at an incident electron energy of 180 eV for different coverages of halocarbons adsorbed at 25 K either on Ru(0001) or on 5 ML D_2O. These dependencies are normalized to the values detected for an undamaged film. The cross-sections for halocarbon decomposition are indicated in figure 19, and corresponding solid lines are exponential fits assuming first-order decay. The plot shows only a modest increase of decomposition rate for both halocarbons on water ice of ~2–3 × compared to adsorption on Ru(0001) as indicated by the different slopes for 1 ML CF_2Cl_2 (figure 19(a)) and 1 ML CCl_4 (figure 19(b)) adsorbed on Ru(0001) and on the ice surface (see section 5). The kinetic data of figures 18 and 19 are important as they illustrate that the radiation-induced decomposition rates for CF_2Cl_2 and CCl_4 in H_2O ice matrices do not depend strongly on concentration, nor are cross-sections greatly enhanced by co-adsorption of CF_2Cl_2 or CCl_4 with H_2O ice. At first glance these conclusions seem to be at variance with previous measurements for which large enhancements in electron-stimulated desorption yields and cross-sections for the electron-stimulated decomposition of organohalides adsorbed on ice films have been reported [28, 30, 31, 70]. This is addressed in section 5.3.

5. Discussion

This following is a discussion of the experimental data presented in section 4, focusing on the chemistry and physics of EDPs within condensed films containing halogenated compounds. We consider the effect of a water matrix on electron-driven chemistry and, more specifically, the role of an ASW matrix on the kinetics, dynamics and reaction pathways of halogenated compounds.

5.1. *Interaction of electrons with adsorbed molecules on surfaces*

Measurements of ESD of ions from the surface, for example yields and directions of desorbing ions, provide unique insights into EDPs for the condensed phase. An experimental study of these characteristics sheds light on both the non-thermal processes of condensed species activated by electrons (e.g. dissociation and reactivity of molecules, solvent effects, etc.) and some aspects of adsorbate/substrate and adsorbate/adsorbate interactions (e.g. conditions for ordered assembly of adsorbed molecules). Low-energy ions detected in ESD experiments have very short escape depths, that is they originate in the topmost one or two molecular layers of the condensed film [21]. The ESD ion fragmentation patterns, as well as yields, energy and angular distributions of desorbing species, provide direct information about electron-induced processes in molecules trapped below the surface. Despite the sensitivity to processes at the outer surface, ESD can provide a 'window' into radiation chemistry that occurs in the bulk of the film. The molecular fragments detected in ESD (and the radical products left behind on the surface) are similar to those that form in the bulk during irradiation.

5.1.1. *Alignment of halogenated molecules on Ru(0001)*

In many cases, the bond directions of adsorbed molecules exhibit preferred orientations. In section 4.1 we showed that analysis of the angular distributions of ions desorbing under electron irradiation is useful for identifying molecular orientation and bond directions. This has important implications for understanding the fundamental aspects of adsorbate/substrate interactions.

The ESDIAD patterns shown in figures 2 and 3 are interpreted as indicating that both SF_6 and CF_2Cl_2 molecules bind to the hexagonal Ru(0001) surface via three halogen atoms (figure 20), similar to earlier findings for CCl_4 [91, 92]. For SF_6 it is also concluded that there is no preferential azimuthal orientation of the molecules upon adsorption at 25 K [40, 41]. This observation indicates the presence of many local minima in the adsorption potential of deposited SF_6 molecules. The global potential minimum is reached only when sufficient thermal energy is imparted to the surface (e.g. via annealing), leading to irreversibly ordered SF_6 with S–F bonds aligned along $[10\bar{1}0]$ crystallographic directions of Ru(0001) [40, 41] (figure 20). This conclusion is based on analysis of hexagonal F^+/F^- ESDIAD patterns for SF_6 (figure 2) and LEED images for the substrate.

In comparison with the adsorption geometry of CF_2Cl_2, CCl_4 and SF_6, phosphorus trifluoride (PF_3) binds to Ru(0001) via the phosphorus atom with three P–F bonds pointing away from the surface in off-normal directions [103]. Angular distributions of F^+ ions for PF_3 reveal halo and hexagonal patterns similar to those observed for SF_6. However, the coverage dependency of PF_3 ESDIAD patterns and also their reversible dependence upon temperature change are interpreted in terms of freely rotating molecules, whose rotation is hindered by increasing coverages (steric hindrance) and/or decreasing temperature [103, 104].

5.1.2. *Composition of anion fragments in ESD from adsorbed halogenated molecules*

Both anion and neutral fragmentation patterns observed in ESD from CF_2Cl_2/H_2O films and from a neat CF_2Cl_2 layer on Ru(0001) were presented in section 4.2 (figures 6 and 7). The negative ion desorption cross-sections are small compared to those for dissociation of the parent molecules. The anions reported for gaseous

Downloaded At: 16:25 21 January 2011

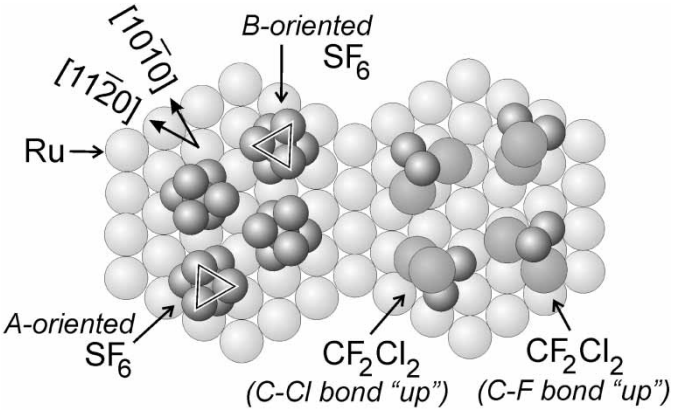

Figure 20. Sketch illustrating the adsorption of SF_6 and CF_2Cl_2 on Ru(0001) at 25 K as established by ESDIAD measurements. Note that the adsorption sites are a pictorial representation because adsorption sites cannot be determined by ESDIAD. Both molecules adsorb on the surface by three halogen atoms. Three 'outer' S–F bonds of the SF_6 molecule point away from the surface in an off-normal direction. The azimuthal orientations of the S–F bond coincides with the [10$\bar{1}$0] crystallographic direction of the substrate where the coexistence of two domains (A- and B-oriented) is justified. The CF_2Cl_2 molecule contacts the surface in random azimuthal orientations either via two Cl atoms and one F atom or via one Cl and two F atoms with nearly equal probability. The fourth C–F (or C–Cl) bond is oriented along normal to the surface.

Downloaded At: 16:25 21 January 2011

CF_2Cl_2 are Cl^-, F^-, FCl^- and Cl_2^-, where Cl^- is the dominant ion fragment [46]. In contrast to the gas phase, the total detected F^- yield for low-energy electron excitation in the condensed phase considerably exceeds the Cl^- yield (see figure 6). Because of the low kinetic energy of Cl^- ions, the majority of the Cl^- ions remain trapped on the surface as they do not have sufficient kinetic energy to overcome the polarization barrier and desorb. In particular, Meinke [68], Hedhili *et al.* [69], and Langer *et al.* [105] did not detect significant Cl^- yields for electron energies < 1 eV. These studies differ from an earlier report by Illenberger [25], for which a significant Cl^- signal is reported even for electron energies < 1 eV.

In addition to Cl^-, F^-, FCl^- and Cl_2^- fragments, the data in figures 6(i) and 6(ii) also reveal the desorption of F_2^- and CF^- ions from both neat CF_2Cl_2 and Freon/water layers. Note that the F_2^- ion has not been reported in the gas-phase dissociation of CF_2Cl_2; however, F_2^- has been detected in studies of other gaseous and adsorbed molecules [92, 106]. For multilayer CF_2Cl_2, the formation of F_2^- from two neighbouring molecules might be expected to have higher probability than its formation from a single adsorbed molecule. For the formation of F_2^-, it is necessary to break two C–F bonds and form an F_2 species in a configuration that is sufficiently repulsive for desorption to occur. The detailed mechanisms for the formation and the desorption of F_2^-, Cl_2^-, CF^- and ClF^- anions, however, are not understood.

5.1.3. *Effect of H_2O on halide anion yields in ESD from CF_2Cl_2 on Ru(0001)*

In section 4.2 we showed data (figure 4) that illustrate the enhancement of anion (Cl^-, F^-) yield in ESD from CF_2Cl_2 co-adsorbed with polar molecules (NH_3, H_2O, CH_3OH) on Ru(0001), a topic that has been intensively studied during the past several years [14, 28, 30, 31, 70]. Earlier ESDIAD measurements of anion

enhancement [28, 30, 31] have been recently reproduced and verified using an ESD QMS technique [70]. The anion enhancement effect is more pronounced for lower Freon coverages, and is greater for Cl^- than for F^-. The role of the co-adsorbed molecules is more intriguing: co-adsorption with polar molecules leads to greater anion yield (in order(s) of magnitude) than with non-polar molecules; however, the greatest enhancement is observed for ammonia, a molecule with smaller dipole moment than, for instance, water (in the ground state at RT, $\mu(NH_3) = 1.47$ D [107] and $\mu(H_2O) = 1.85$ D [108]; note: $\mu(CF_2Cl_2) = 0.51$ D ([109]). A detailed discussion of the characteristics of giant enhancement in anion ESD yields is given elsewhere [30, 70].

The current explanation of the anion enhancement observed during ESD of CF_2Cl_2 adsorbed on polar molecular ice films is based on the proposal that the DEA to CF_2Cl_2 may be affected by increasing the concentration and lifetime of low-energy electrons in the co-adsorbed film, that is decreasing the rate at which the secondary electrons tunnel back to the metal [28, 30, 31]. Upon injection of secondary electrons from the metal sample into the polar layer, it has been proposed that some of the low-energy electrons may become 'trapped' and solvated by the polar molecules such as water. The trapped electron can then propagate through the polar molecular ice to a CF_2Cl_2 molecule and form a vibrationally excited intermediate state ($CF_2Cl_2{}^{*-}$) that can then dissociate, producing Cl^- or F^- ions. An estimation of the energy balance required by this process [30] indicates that fully solvated electrons cannot be responsible for the phenomena observed [32]. Recently, it has been proposed that ~0 eV electrons are temporarily localized as precursors of the fully solvated state in polar molecular ices [32, 35, 110]. The precursor is a transient state whose energy is above or near the vacuum level, that is an excited state of the solvated electron or 'hot pre-solvated electron.' Electrons in this state are very mobile and may react rapidly with molecules that have a positive electron affinity (EA); the EA of CF_2Cl_2 is +0.4 eV [111].

A consequence of the mechanism described above is an increase in the DEA cross-section for CF_2Cl_2 adsorbed on/in polar molecule ices (e.g. on water or ammonia ice surfaces) as compared to the neat Freon layer. The hypothesis is supported by the charge trapping experiments performed by Sanche and colleagues [32, 35, 112]. A large increase in the charge trapping coefficient for 0.1 ML CF_2Cl_2 deposited on a thick (5 ML) H_2O film supported by a 10 ML Kr layer has been observed upon irradiation of the layer by low-energy electrons (<10 eV) [32]. The increase is attributed to accumulation of solvated Cl^- anions as a result of the increased efficiency of the DEA process in the presence of H_2O. This behaviour can be compared with ESD experiments [70] in which an enhancement of anion (Cl^-, F^-) yields is observed for CF_2Cl_2 co-adsorbed with very thin H_2O (NH_3) films on metal substrates, where the maximum yields are found at 1–2 ML H_2O (NH_3); the anion ESD signal then decreases as the film thickness increases. This observation indicates that the proximity of the metal substrate plays a key role in the anion enhancement. However, in both ESD and charge-trapping experiments described above, the connection of the measured quantities to DEA cross-sections is an indirect one: the rate of dissociation of CF_2Cl_2 is not measured directly, but is inferred. The results of direct measurements of electron-induced dissociation of two halocarbon molecules, CF_2Cl_2 and CCl_4, co-adsorbed with water ice are described in section 4.8 and are considered further in section 5.3, where we show that H_2O-induced enhancements in total dissociation cross-sections are considerably smaller than ESD anion and

Downloaded At: 16:25 21 January 2011

charge-trapping enhancement effects. We also suggest why the charge-trapping and ESD anion measurements may not give accurate magnitudes of cross-sections for electron-induced dissociation (via DEA) of Freon co-adsorbed with H_2O.

5.2. *Structure of halocarbon/water films*

As described in section 3.3 we mimic liquid H_2O by using vapour-deposited thin films of ASW condensed onto cold (25–100 K) substrates. ASW is a 'frozen', metastable, supercooled liquid [78, 95] whose density and pore structure depend on the substrate temperature and deposition angle (i.e. the angle between the vapour beam and the substrate normal). For our usual conditions in TPD experiments, that is deposition of H_2O vapour onto a substrate held at 25 K using a gas doser capped with a microcapillary array (normal incidence), a smooth non-porous film with density $\sim$1 g cm^{-3} is expected [75, 77]. Our recent studies indicate that co-deposition of halocarbons with H_2O vapour at 25 K also leads to an ASW matrix [36, 71]. ASW undergoes a phase transition to crystalline ice at $\sim$155 K (H_2O) or $\sim$165 K (D_2O). The phase change can be identified in TPD spectra of multilayer ASW, because the vapour pressure of ASW is higher than that of crystalline ice. It is generally agreed that ASW is a good model system for studying radiolytic processes driven by low-energy electrons in liquid water, with the caveat that diffusion and relaxation processes in ASW are considerably slower than in liquid water [78].

Downloaded At: 16:25 21 January 2011

Halocarbons adsorbed on top of a metal surface (e.g. CF_2Cl_2 and CCl_4 on Ru) are weakly bonded to the substrate [37]. The corresponding desorption peak temperatures are consistent with physisorbed states [27, 91]. However, halocarbons bind even more weakly to the surface of dense water ice films. Thus for CF_2Cl_2 deposited on a H_2O surface, the peak desorption temperature (solid curve in figure 5(a)) shifts to a lower value vs. CF_2Cl_2 on Ru (dashed curve in figure 5(a)), confirming that the binding of Freon to a water ice surface is weaker than to Ru. Similarly, a decrease in the desorption temperature from $\sim$165 to $\sim$135 K has been observed for CCl_4 adsorbed on a D_2O ice surface vs. Ru(0001) [91]. By contrast, halocarbons incorporated into a water ice matrix exhibit increased thermal stability. For example, a mixed Freon/water film (figure 5(b)) reveals desorption of CF_2Cl_2 both from the D_2O ice surface ($\sim$110 K) and from the bulk of the film ($\sim$165 K). The peak desorption temperature of Freon from the bulk is higher than the desorption temperature of Freon from Ru (0001) ($\sim$140 K; see dashed curve in figure 5(a)). This indicates that the release of the majority of the molecules from the water matrix is blocked by the ASW layer, which is thermally more stable than Freon. The escape of halocarbon molecules from the film is facilitated by water crystallization when a number of defects producing connected pathways in the ice layer are formed.

The TPD blocking effect (i.e. inhibition of Freon desorption by a water ice overlayer) has been observed earlier for halocarbons (CCl_4 [93], CD_3Cl [113], CF_2Cl_2 [37]), N_2 [114] and SF_6 [71] under thick water overlayers, where the release of the trapped molecules occurs spontaneously in a very narrow temperature range (several degrees K) corresponding to ASW crystallization. This phenomenon is known as 'molecular volcano' desorption [93]. In the case of a Freon/ice mixture, where incorporated halocarbon molecules are distributed randomly within the film, a small fraction of molecules trapped in the topmost surface layers is able to escape before the water phase transition, as water molecules desorb. This is indicated by the relatively broad leading edge of the desorption profile in figure 5(b) compared to the

sharp peak due to Freon desorption from beneath the ice overlayer [37]. Variations in the film thickness (with the concentration of the dosing mixture being conserved) leads to a proportional change in the total area of the CF_2Cl_2 and D_2O TPD curves, while the number of CF_2Cl_2 molecules at the ice surface remains nearly constant (within ~20% accuracy) [37]. This implies that during thermal annealing, segregation of CF_2Cl_2 to the surface of the D_2O ice does not occur, and that CF_2Cl_2 is distributed homogeneously within the film.

5.3. *Chemical reactions initiated by ionizing radiation*

In this section, we use the CF_2Cl_2/H_2O system as an illustrative example of the reaction kinetics and mechanisms of EDPs. Chemical reactions observed in the present study are postulated to involve low-energy secondary electrons generated within the halocarbon/H_2O (ice) film and from the metallic substrates as a result of electron-beam/X-ray irradiation.

5.3.1. *Role of low-energy secondary electrons*

In a solid, incident high-energy particles (electrons or photons) create a broad, continuous distribution of hot electrons [115]. As an energetic electron moves through the solid, it undergoes a series of elastic and inelastic collisions, losing its initial energy and producing a number of low-energy secondary electrons. Even for the case of high-energy electrons (20 keV) interacting with liquid water, Monte-Carlo simulations indicate that about 90% of the electrons ejected by both primary electrons and successive generations of secondary electrons have low energies, less than 20 eV [116].

Although the ultimate energy distribution of secondary electrons is expected to be similar for incident X-rays and energetic electrons, the spatial or depth distribution of secondary electrons within the film will depend on the penetration depth of the incident high-energy particle. The penetration depth differs substantially for high-energy photons (1253.6 eV/1486.6 eV X-rays) and lower-energy electrons (a few hundred eV). X-ray penetration depths are ~1–10 μm [42], whereas the effective range of a 200 eV electron (i.e. distance to lose most of its initial energy) is ~2–10 nm (greater than the inelastic mean free path) [117]. Thus, the non-thermal processes induced by electron beams (~200 eV) affect thinner, near-surface layers of a solid or condensed film, whereas processes initiated by more penetrating X-ray photons take place in thicker, nearly bulk layers. Because of relative source intensities (X-ray source vs. electron gun) in our experiments, the flux of photoelectrons is generally less than that of incident electrons, so that processes induced by incident electrons occur with higher rates than for X-rays.

5.3.2. *Electron-stimulated decomposition of the halocarbon parent*

As we highlight in section 3, the interaction of low-energy electrons (~0 eV) with gas-phase CF_2Cl_2 leads predominantly to C–Cl bond cleavage and production of Cl^- and a trihalomethyl radical (CF_2Cl [24, 44, 46, 47]. Indeed, the DEA process is thought to be responsible for carbon–halogen bond cleavage in the radiolysis of organohalides [118]. Our experimental data also indicate that DEA activated by low-energy secondary electrons is the major mechanism of halocarbon decomposition in ice films [14, 27], based on the observation that bond-breaking in condensed CF_2Cl_2 is selective towards C–Cl bond cleavage. This is clearly seen from our XPS data (figure 16), which indicate the dominance of Cl^- production during the initial

Downloaded At: 16:25 21 January 2011

stages of irradiation. Another important observation is that both X-rays and electrons lead to decomposition of halocarbons and produce the same chemistry. Although X-ray radiation can dissociate molecules by creating core holes, the cross-sections for such processes are much smaller than the typical cross-section for DEA by low-energy electrons [46]. Thus, DEA mediated by low-energy secondary electrons is the dominant initial bond-breaking process in all halocarbon-containing films discussed in this review.

5.3.3. *Rates of halocarbon decomposition*

Recent studies of adsorbed halocarbons (CF_2Cl_2, CCl_4) [14, 28, 30, 32, 33, 70, 112] indicate enhancements of anion ESD yield and charge trapping coefficient when the halocarbons are co-adsorbed with water (see sections 4.2 and 5.1.3 for details). The effects are attributed mainly to an increase in DEA cross-sections [14, 28, 32]. However, both of these experimental approaches deliver only indirect information about DEA cross-sections. The key assumption in interpretation of the charge-trapping data is that DEA of CF_2Cl_2 at near 0 eV electron energies results in the formation of trapped Cl^- [32]. However, a similar effect might also be observed experimentally if the charge is trapped mainly as a stable, undissociated molecular anion, $CF_2Cl_2^-$, so that the DEA cross-section is *not* enhanced substantially. This point requires further investigation. Similarly, the ESD anion enhancement experiments [30, 33] have been interpreted in terms of an increase in DEA cross-section, associated with trapped pre-solvated electrons at the H_2O surface (see section 5.1.3). This, also, may not be a complete explanation: the enhanced anion desorption yield may also be influenced by several other effects [28, 30, 119] due to the presence of the H_2O co-adsorbate; for example, changes in anion neutralization rates (electron hopping times) that increase ion lifetimes [120].

With the aim of clarifying the true magnitudes of DEA cross-sections, the focus of a recent study [37] has been an attempt to measure directly the rate of adsorbed halocarbon decomposition under electron irradiation. This experiment excludes ambiguities in the determination of DEA cross-section due to additional factors, for example image potential and neutralization processes affecting anion yields [14, 28], or an unrecognized stable anion (e.g. $CF_2CL_2^-$) in charge-trapping experiments [32].

To ascertain the effect of H_2O on the kinetics of decomposition of the halocarbon molecules, TPD data have been obtained for thin films (1.4 nm) [121], which ensures a more uniform distribution of secondary electrons than in the case of thicker films (>30 nm) [37]. In figure 19 the normalized TPD peak areas for CF_2Cl^+ and CCl_3^+(corresponding to the dominant fragmentation ions for CF_2Cl_2 and CCl_4 respectively) are plotted as a function of electron irradiation. The straight lines in the semilogarithmic plots are proportional to the cross-section for dissociation of the CF_2Cl_2 and CCl_4 molecules, assuming first-order kinetics. The increased slope for 1 ML CF_2Cl_2 (figure 19(a)) and 1 ML CCl_4 (figure 19(b)) adsorbed on the water ice surface vs. Ru(0001) implies an increase in the decomposition rate for both halocarbons. By contrast, the initial coverages of CF_2Cl_2 and CCl_4 on 5 ML D_2O only weakly affect the decomposition cross-sections. These cross-sections are also in general agreement with the values for halocarbon/water mixed layers calculated from the attenuation of corresponding parent C 1s XPS peaks (see figure 10 in [37]). In a recent, more detailed study [71], where fractional monolayers of CF_2Cl_2 were adsorbed on H_2O (ice) films with variable thicknesses, we observed a steady

Downloaded At: 16:25 21 January 2011

increase in the Freon dissociation cross-section with increasing water layer coverages in the range from fractional ML to several ML. By contrast, the cross-section for neat Freon adsorbed on a Ru surface [71] was found to be independent of the CF_2Cl_2 film thickness in the range from fractional ML to several ML of CF_2Cl_2 (cf. data points for 1 ML and 4 ML of neat Freon on Ru in figure 19(a)). Thus, the increase in cross-section of Freon observed on water ice surfaces cannot be attributed simply to the relaxation of de-excitation processes by increasing the spacing of a molecule from the metal surface. A quantitative estimation shows that the cross-section for decomposition increases by a factor of ~2 (from 3.6×10^{-16} to $8.2 \times 210^{-16}\,cm^2$) for Freon and by a factor of ~4 for carbon tetrachloride (from 4×10^{-16} to $15 \times 10^{-16}\,cm^2$) on ~5 ML water ice surfaces, as compared to a metal substrate. Overall, the decomposition cross-section of CF_2Cl_2 is smaller than that of CCl_4.

While TPD data imply detectable increases in the decomposition cross-sections for CF_2Cl_2 and CCl_4 in the presence of water, the magnitudes are much smaller than in anion ESD yield experiments (e.g. ~100 × for the CF_2Cl_2 Cl^- ESD yield) (figure 4) [30, 122]. This observation is also supported by RAIRS data in figure 18 (measured for thick ~50 nm Freon/water films), which exhibit no systematic dependence of Freon decomposition rate (under X-rays) on the initial chemical composition of the mixed CF_2Cl_2/H_2O films (for Freon/water ratios (≤0.3) [36]. Thus, the present direct measurements of total dissociation cross-sections indicate that, in contrast to the results of refs [30, 32], the effect of H_2O on the rate of CF_2Cl_2 decomposition is either weak (TPD data for thin films, figure 19) or absent (RAIRS data for thick films).

As indicated above in this section, a comparison of the anion ESD yield experiments [14, 30] and the charge-trapping experiments [32] with TPD/XPS/RAIRS studies of figures 18 and 19 [36, 37] is not straightforward. The ESD of Cl^- ions is a multiple-step process involving both the dissociation of the parent CF_2Cl_2 molecule and desorption of the Cl^- ions. In order for an ion to desorb, it must be stable for a sufficient amount of time after formation and must possess enough translational kinetic energy to desorb from the surface. Typically, only a very small fraction of ions formed desorbs from a surface ($\sim 10^{-7}$) [45, 52, 123]. Moreover, the presence of a water layer may influence the anion desorption lifetime, increasing the fraction of ions that survive to desorb. Note also that an incident electron energy of ~200 eV is used in the TPD/XPS/RAIRS and also in the ESD yield experiments, while near 0 eV electrons were used by Lu and Sanche in charge-trapping measurements [32, 35]. In the latter experiments, however, the authors were not able to distinguish conclusively between a trapped Cl^- fragment and stabilized$CF_2Cl_2^-$. The increase in the charge trapping might, for instance, indicate an increase of the electron attachment process and longer lifetime of $CF_2Cl_2^-$, but not necessarily indicate an enhancement of CF_2Cl_2 decomposition rate and Cl^- formation. This is an important open issue that requires further study.

5.4. *Electron-stimulated reactions of organohalides in water (ice)*

The interaction of ionizing radiation (~200 eV electrons or Al Kα X-rays) with molecular CF_2Cl_2 or CCl_4 co-adsorbed with water at low temperatures (25–100 K) leads to electron-stimulated decomposition of both organohalides. Damage fragments and products of subsequent chemical reactions detected in the films include

Downloaded At: 16:25 21 January 2011

Cl^- and F^- anions, H_3O^+, COF_2 (for CF_2Cl_2), $COCl_2$ (for CCl_4), C_2Cl_4 (for CCl_4) and CO_2. In this section we use CF_2Cl_2/H_2O and CCl_4/H_2O systems as illustrative examples of the electron-driven chemistry that occurs within mixed component systems CX_4 (X=Cl, F, Br, I) organohalide+water. In particular, this section focuses on the chemistry initiated by X-ray irradiation, followed by a comparison with the effects of electron-beam irradiation.

5.4.1. *X-ray induced reactions of CF_2Cl_2/H_2O*

As described in sections 5.3.1 and 5.3.2, the X-ray induced chemistry is caused mainly by secondary electrons; the interaction of X-rays with CF_2Cl_2 adsorbed on water (ice) or in the bulk of water ice (cf. figure 9 and 16) results in the formation of carbon-containing species COF_2, CO_2 and a polymeric CF_xCl_y film as well as hydronium ions (H_3O^+) and F^- and Cl^- anions. These transformations have been identified by RAIRS (figure 9) and XPS (figure 16) measurements. Although the radiation chemistry of halogenated hydrocarbons in the presence of water is an extremely complicated subject, a number of studies have shown that the dominant reaction products can typically be described by a small subset of reaction steps [36, 38, 39]. Scheme 1 shows the principal chemical reaction pathways that we believe are responsible for production of stable carbon-containing and charged species during the X-ray irradiation of CF_2Cl_2/H_2O (ice) films.

Downloaded At: 16:25 21 January 2011

The production of Cl^- anions results from the initial DEA of the parent CF_2Cl_2 molecule and the subsequent decomposition of the $CF_2Cl(OH)$ intermediate. By contrast, F^- production is associated largely with the decomposition of the carbonyl difluoride (COF_2) intermediate. As a result, the Cl^- anion concentration during the initial stages of the X-ray irradiation is much greater than that of the F^- anion (figure 13). Despite the formation of Cl^- and F^- anions in the film, the total integrated Cl 2p and F 1s XPS areas remain almost constant during X-ray irradiation. This indicates that during X-ray irradiation of CF_2Cl_2/H_2O, both Cl^- and F^- anions are efficiently solvated (trapped) in the film. The observed lack of significant anion desorption into vacuum under these conditions is thought to be a result of their low mobility within the ice film under low-temperature conditions.

Carbonyl difluoride (COF_2) is postulated to form as a result of reactions associated with the $\cdot CF_2Cl$ intermediate produced in the initial DEA process and hydroxyl radicals, the latter generated by electron-stimulated reactions of H_2O [36]:

$$\cdot CF_2Cl + \cdot OH \rightarrow CF_2Cl(OH) \tag{5a}$$

$$CF_2Cl(OH) + H_2O \rightarrow CF_2O + H_3O^+ + Cl^- \tag{5b}$$

The observation in RAIR spectra (figure 9) that COF_2 is the exclusive carbonyl dihalide species indicates that during the initial stages of the reaction, C–Cl rather than C–F bond-breaking events dominate. Thus, the formation of COF_2 is a direct consequence of the C–Cl bond cleavage during the DEA of CF_2Cl_2 and the subsequent decomposition of the $CF_2Cl(OH)$ intermediate to produce COF_2. The absence of any COFCl production associated with the reactivity of the $\cdot CF_2Cl$ intermediate is ascribed to the greater thermodynamic stability of COF_2 arising from the greater C–F vs. C–Cl bond strength. This results in COF_2 being $\sim$200 kJ mol^{-1} thermodynamically more stable than COFCl [124].

Figures 9 and 10 illustrate that COF_2 is not stable to continued X-ray irradiation but behaves as an intermediate, being both produced and destroyed by electron-

stimulated processes. Indeed, the production of CO_2 is postulated to occur as a result of the electron-stimulated degradation of COF_2 (scheme 1) through a mechanism analogous to the one responsible for COF_2 production from CF_2Cl_2:

$$COF_2 + e^- \rightarrow \cdot COF + F^- \tag{6a}$$

$$\cdot COF + \cdot OH \rightarrow\rightarrow CO_2 + H_3O^+ + F^- \tag{6b}$$

The origin of the hydronium ions (H_3O^+) observed in RAIRS stems from the decomposition of the $CF_2Cl(OH)$ and $COF(OH)$ transient intermediates, during the formation of COF_2 and CO_2 respectively (equation (5b)).

In addition to the discrete molecular fragments and ions produced, C 1s XPS measurements in figure 14 indicate that a partially halogenated CF_xCl_y film is also produced during X-ray irradiation. The formation of a CF_xCl_y film is postulated to arise from carbon–carbon coupling reactions involving carbon-containing radicals [36]. Experimentally, the formation of this partially halogenated film is evidenced by a broadening in the C 1s region after X-ray irradiation for organohalide-rich CF_2Cl_2/H_2O (figure 14(ii)) and CD_2Cl_2/H_2O films (figure 17).

Once formed, the polymeric CF_xCl_y film exhibits greater thermal stability compared to the various molecular fragments, evidenced by the presence of residual carbon, chlorine and fluorine after the sample has been warmed to room temperature (well above the desorption temperature of CO_2, COF_2 and HCl). Further annealing of the CF_xCl_y film to approximately 560 K results in thermal dissociation of the C–Cl and C–F bonds to leave a predominantly graphitic overlayer, evidenced by the dominance of a single peak at ~285 eV in the C 1s region and (figure 14(v)). Other studies show that carbon–coupling reactions also occur in hydrocarbon films under the influence of ionizing radiation [125, 126]. Nakayama *et al.* [127] investigated

Downloaded At: 16:25 21 January 2011

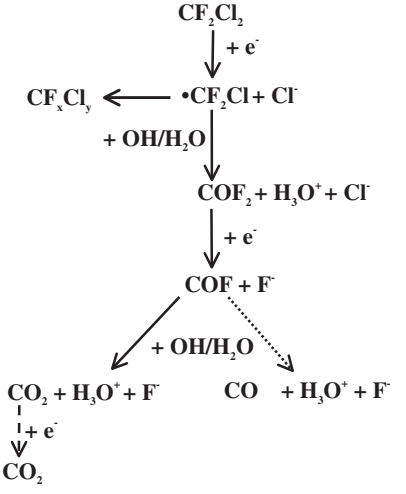

Scheme 1. Postulated dominant electron-stimulated reactions for the carbon-containing fragments in CF_2Cl_2/H_2O films. Solid arrows indicate pathways for both X-ray and electron-beam irradiation while the dotted arrows indicate reactions only accessible under high electron flux conditions. The dashed arrow represents the electron-stimulated desorption of carbon dioxide.

the low-energy electron-induced production of neutral species from CF_2Cl_2 films. Post-irradiation TPD was used to detect various C_2 ($C_2F_yCl_z$) type species. In another example, Feldman *et al*. [125] investigated the effect of radiation-induced degradation of heptanes using IR spectroscopy. Numerous hydrocarbon degradation products were observed by IR including methane, vinyl- and *trans*-vinylene-type olefins. Similarly, Swiderek *et al*. [126] studied reactions of cyclopropane using low-energy electrons (15 eV), which resulted in the formation of longer chains and various conjugated products.

5.4.2. *Influence of the film's chemical composition on product partitioning*

Differences in the product partitioning as a function of the film's initial chemical composition can largely be correlated with the fate of the $\cdot CF_2Cl$ intermediate produced as a result of the initial C–Cl bond cleavage. In dilute films, reactions of the $\cdot CF_2Cl$ intermediate with oxygen-containing species dominate, and lead to the formation of COF_2 and then CO_2 (figure 9). Indeed, CO_2 is essentially the exclusive carbon-containing species ultimately produced in dilute films where the initial $CF_2Cl_2 : H_2O$(ice) ratio is low ($\sim$1 : 10). This is indicated by the XPS data shown in figure 13, which shows that nearly all of the carbon initially present as CF_2Cl_2 (C 1s peak at $\sim$293 eV) is eventually converted into CO_2 (C 1s peak at 291 eV); this conclusion is corroborated by RAIRS results shown in figure 9.

By contrast, during X-ray irradiation of CF_2Cl_2-rich films where the $CF_2Cl_2 : H_2O$ ratio is high ($\sim$1:1), carbon–coupling reactions become significant, as evidenced by the production of the partially halogenated CF_xCl_y polymeric film (e.g. figure 14). The increased probability of carbon–carbon coupling reactions decreases the amount of COF_2 and CO_2 produced in the film (scheme 1). This is evidenced by the IR results shown in figure 15, where the concentrations of CO_2 and COF_2 decrease (after a fixed period of X-ray irradiation) with higher initial CF_2Cl_2 concentrations in the film, although the rate of CF_2Cl_2 loss remains constant (see figure 18).

Figure 18 reveals that over the concentration range studied in the present investigation, there is no significant difference in the rate of CF_2Cl_2 depletion. However, figure 16 indicates that in more H_2O-rich films, after a fixed period of X-ray irradiation, greater fractions of Cl and F are converted into Cl^- and F^-. Thus, while Cl^- ions are always generated during the initial DEA process, the production of subsequent halide ions (Cl^- or F^-) is correlated with the fate of the $\cdot CF_2Cl$ intermediate. In dilute films, the dominant reaction channels involve the production of Cl^- during COF_2 formation, followed by F^- during CO_2 production (scheme 1). By contrast, the fate of any carbon-containing radical intermediate in more $CF_2Cl_2^-$ rich films is likely to involve carbon–carbon coupling reactions leading to the production of a CF_xCl_y overlayer and a lower concentration of Cl^- and F^- ions. Although this model provides a qualitatively correct interpretation of the results, experimental data reveal that for concentrated films, the total Cl^- anion yield is < 0.5 despite the predominance of Cl^- formation in the initial DEA of CF_2Cl_2. One possible explanation for this discrepancy may lie in the role of surrounding water molecules in solvating Cl^- and F^- anions, preventing further chemical transformations in more dilute films. In particular, a simple statistical model has been used to describe the correlation between the degree of isolation of a Freon molecule and the formation of a stable (i.e. long-lived) chloride anion [37].

Downloaded At: 16:25 21 January 2011

5.4.3. *Influence of film structure and composition on electron-stimulated reactions in the CF_2Cl_2/water (ice) films*

When background dosing conditions are used to generate the CF_2Cl_2/H_2O (ice) films (prevalent for the XPS and RAIRS studies), the initial film is expected to consist of microporous amorphous ice that contains CF_2Cl_2 at the surface as well as trapped within the ASW matrix [73, 74, 128]. Electron-stimulated reactions between oxygen-containing species such as hydroxyl radicals and fragments of CF_2Cl_2 dissociation such as $\cdot CF_2Cl$ are most likely to occur at the interfacial regions between domains of H_2O and CF_2Cl_2 within the amorphous ice matrix. By contrast, carbon–carbon coupling reactions are expected to occur for CF_2Cl_2 molecules initially present as part of a discrete cluster within the film. From these considerations it is clear that CO_2 and COF_2 production will be favoured in dilute films where, on average, CF_2Cl_2 molecules are surrounded by a large number of adsorbed H_2O molecules. By contrast, the carbon–carbon coupling process will predominate in more concentrated films where extensive CF_2Cl_2 clustering within the amorphous film is anticipated.

5.4.4. *X-ray stimulated reactions of CCl_4/H_2O*

XPS and RAIRS experiments on reactions within CCl_4/H_2O (ice) films during X-ray irradiation have revealed the formation of CO_2, $COCl_2$, C_2Cl_4, H_3O^+ and Cl^- anions that are solvated in the film at ~100 K [38, 39]. In general, the proposed reactions of CCl_4 are analogous to those of CF_2Cl_2 (both are CX_4 organohalides): low-energy secondary electrons cause decomposition via DEA to produce a trihalomethyl ((CX_3) intermediate. Scheme 2 summarizes the main subset of reactions that are thought to be responsible for the observed carbon-containing products observed during X-ray irradiation of CCl_4/H_2O(ice) films.

Additional support for the idea that DEA is the dominant initial step is provided by calculated rates for carbon tetrachloride decomposition in air plasmas, which indicate that the DEA process is favoured by several orders of magnitude over any other potential reactions such as hydroxyl ((OH) radical addition [129]. Reactions between the trichloromethyl ($\cdot CCl_3$) radical generated as a result of the initial DEA process and hydroxyl radicals are postulated to be responsible for the production of phosgene, whose subsequent electron-stimulated decomposition produces CO_2, analogous to the reactions of CF_2Cl_2. Thus, in dilute CCl_4/H_2O films (CCl_4/H_2O ratio < 0.1) CO_2 is the dominant carbon-containing fragment while carbon–carbon coupling processes become more important for more CCl_4^- rich films. Although reactions of CF_2Cl_2 and CCl_4 are generally comparable, there are some differences. In contrast to CF_2Cl_2/water films, where there is no evidence of difluorocarbene as a discrete molecular fragment, C_2Cl_4 was routinely observed in CCl_4^- rich films due to carbon–carbon coupling reactions associated with the dichlorocarbene ($:CCl_2$) intermediate (see figures 8 and 12).

5.4.5. *Influence of the irradiation source: X-ray vs. electron-beam irradiation*

An important observation is that reaction products observed by RAIRS, XPS and TPD measurements on CF_2Cl_2/H_2O and CCl_4/H_2O films are largely independent of the radiation source (~200 eV electrons vs. X-ray photons). This is perhaps most clearly indicated by TPD results shown in figure 8 of electron beam-induced products observed for CCl_4 and CF_2Cl_2 adsorbed on water and the analogous X-ray and electron-beam IR data shown in figures 9, 10 and 12. For example, TPD

Downloaded At: 16:25 21 January 2011

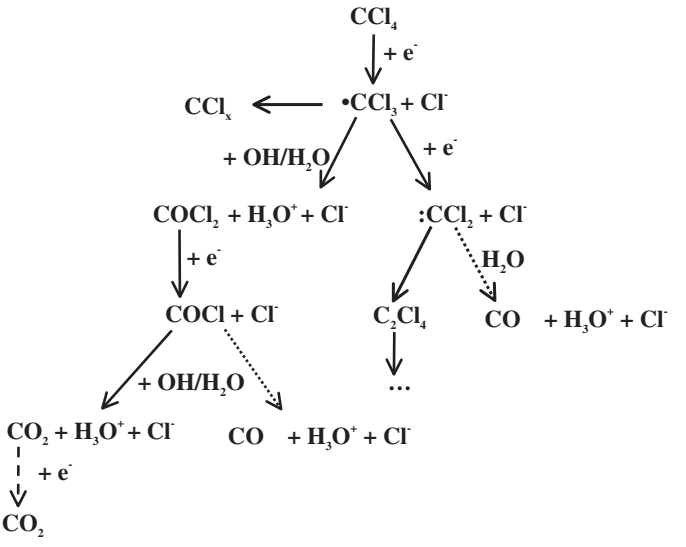

Scheme 2. Postulated dominant electron-stimulated reactions for the carbon-containing fragments in CCl_4/H_2O films. Solid arrows indicate pathways for both X-ray and electron-beam irradiation while the dotted arrows indicate reactions only accessible under high electron flux conditions. The dashed arrows represent the electron-stimulated desorption of carbon dioxide.

Downloaded At: 16:25 21 January 2011

shows an increase in 47 amu (COF_2) and 63 amu ($COCl_2$) signals after electron-beam irradiation of CF_2Cl_2/H_2O or CCl_4/H_2O films, respectively, consistent with RAIRS assignments of intermediate COX_2 species in these two systems. Similarly, RAIRS and TPD measurements both demonstrate the production of C_2Cl_4 during electron-beam or X-ray irradiation of CF_2Cl_2/H_2O films and the absence of C_2F_4 production during reactions involving CF_2Cl_2/H_2O films [37]. Furthermore, a comparison of X-ray and electron-beam irradiated CF_2Cl_2/H_2O films measured by XPS (figures 13 and 16) illustrates that both sources lead to the formation of Cl^- and F^- anions. The similarity between the reaction products observed in these studies serves to further highlight the crucial role that low-energy secondary electrons play in the decomposition of organohalides in these ice films. See also the discussion in sections 5.3.1 and 5.3.2.

Although there are numerous qualitative similarities between the reaction dynamics initiated by X-ray and electron-beam irradiation, there are additional effects observed when higher fluences and electron-beam energies are used. For example, under electron beam conditions when the total electron fluence is higher ($\sim 10\times$), the RAIR intensity plot in figure 10(b) indicates that there is electron-stimulated desorption of CO_2, in contrast to X-ray irradiation where CO_2 remains stable within the film. The desorption of species under these conditions is also supported by XPS results indicating an increase in the Au 4f signal and a corresponding decrease in the C 1s, O 1s and halide (F 1s and Cl 2p) signals under these conditions. Experimental observations indicate that electron-beam irradiation is also accompanied by ESD of charged (O^-, OH^-, H^-) and neutral (CO/CO_2, HCl, O_2, H_2) gas-phase species from the film, as illustrated in figures 6 and 7. The carbon-containing species produced during the electron-beam irradiation of organohalide:-H_2O(ice) films include CO and CO_2. Carbon monoxide, which is not produced

during X-ray irradiation, is postulated to arise from the electron-stimulated decomposition of the COX intermediate:

$$COX_2 + e^- \rightarrow \cdot COX + X^- \quad (7a)$$

$$\cdot COX + e^- \rightarrow CO + X^- \quad (7b)$$

Another possible route for CO production includes the H-atom mediated decomposition of the ·COX intermediate [38]. Figure 7 shows that the CO_2/CO ratio observed in the gas phase increases in dilute films. This is consistent with the proposed routes for CO and CO_2 production (schemes 1 and 2) because both involve sequential reactions involving a carbon and oxygen-containing species. As a result, the decomposition of COX_2 to CO_2 represents a more important pathway in dilute films where the relative H_2O concentration in the film is greatest. By contrast, CO is the dominant carbon-containing gas-phase species observed in organohalide-rich films.

The electron-stimulated decomposition of water also results in desorption of molecular hydrogen and oxygen (figure 7), although the production of these two molecular species is suppressed in $CF_2Cl_2^-$ or CCl_4^- rich films. Although the exact mechanism for hydrogen and oxygen production during electron-stimulated reactions in water (ice) films is unclear, Orlando and co-workers have proposed that molecular oxygen is produced through an HO_2 or H_2O_2 precursor that dissociates upon further electronic excitation, rather than by O atom recombination [83, 84]. A possible explanation for the concentration dependence in the oxygen yield (figure 7) is the greater difficulty in initiating bimolecular reactions involving hydrogen and oxygen-containing species in more concentrated films containing large concentrations of organohalides, given the limited diffusion length of radicals anticipated in these ice films. Another possible explanation for the suppression of oxygen production in films containing a significant concentration of organohalide could lie in the presence of the highly efficient reaction between the trihalomethyl radical and molecular oxygen to produce phosgene [130]:

$$\cdot CCl_3 + O_2 \rightarrow CCl_3OO\cdot \quad (k = 3.3 \times 10^9\ M^{-1}s^{-1}) \quad (8a)$$

$$2CCl_3OO\cdot \rightarrow O_2 + 2CCl_3O\cdot \quad (8b)$$

$$2CCl_3O\cdot \rightarrow COCl_2 + Cl\cdot \quad (8c)$$

The absence of oxygen production during X-ray irradiation is probably a consequence of the fact that very few secondary electrons are expected to be produced with energies near the ~10 eV ionization threshold necessary to produce O_2 from H_2O (ice) films [83, 84]. By contrast, a greater fraction of higher energy secondary electrons are anticipated during electron-beam irradiation with a primary (~200 eV) electron beam.

In summary, similar products are observed in the decomposition of organohalides in water (ice) films independent of the source of excitation (either X-rays or an electron beam); however, during electron-beam irradiation ESD of both charged and neutral fragments is observed, which is associated with erosion of the film. In addition, at higher electron-beam energies and fluxes new reaction products, including molecular O_2 and CO, are also observed.

Downloaded At: 16:25 21 January 2011

5.5. *Influence of the chemical composition of the organohalide on the reaction products observed during electron-stimulated decomposition in water (ice) films*

In this section, we discuss the chemical transformations that occur under the influence of ionizing radiation for the halocarbons $CDCl_3$, CD_2Cl_2 and CH_3I co-adsorbed with water on gold surfaces at ~100 K. For $CDCl_3/H_2O$ films, figure 11 illustrates that the molecular products observed using RAIRS under electron-beam irradiation are $COCl_2$, hydronium ions and CO_2. XPS results (not shown) also confirm the production of chloride anions. Based on radiolysis studies of $CHCl_3$ decomposition in aqueous solutions [131], the initial step in the decomposition of $CDCl_3$ is believed to be DEA, analogous to the reactions of CF_2Cl_2 and CCl_4.

$$CDCl_3 + e^- \rightarrow Cl^- + \cdot CDCl_2 \quad (k = 3 \times 10^{10}\,M^{-1}s^{-1}) \tag{9a}$$

$$CDCl_3 + \cdot OH \rightarrow \cdot CCl_3 + HDO \quad (k = 2 \times 10^{7}\,M^{-1}s^{-1}) \tag{9b}$$

Indeed, our evidence indicates that DEA is the initial step in the decomposition of all of the organohalides studied in the present investigation. In the case of $CDCl_3$, DEA leads to the production of $\cdot CDCl_2$. The decomposition of this intermediate via reactions with ·OH radicals analogous to the reaction pathways outlined for CF_2Cl_2 and CCl_4 would be expected to produce DCOCl, but there is no evidence of this species by RAIRS. Instead we observe the production of $COCl_2$, indicating that there is an efficient route for phosgene production from $\cdot CDCl_3$. This fact reflects the importance of $COCl_2$ as a thermodynamic sink in the decomposition of polychlorinated organohalides, although the mechanistic route for $COCl_2$ production in this system remains unclear. Once formed, $COCl_2$ undergoes electron-stimulated decomposition to yield CO_2. In addition, the difference spectra shown in figure 11 indicate that the loss of ·OH signal intensity is accompanied by the production of hydronium ions as well as the appearance of a new band at 1296 cm^{-1}, which can be correlated with the presence of O–D bonds in partially deuterated hydronium species such as H_2DO^+.

Figure 12 affords a comparison among the different reaction products observed for the various halocarbons studied in this investigation (CF_2Cl_2, CCl_4, $CDCl_3$, CD_2Cl_2, $CDCl_3$ and CH_3I) as a result of electron-beam irradiation. All halocarbons produce CO_2 as a final product, while the CX_4 (CF_2Cl_2, CCl_4) and CHX_3 ($CDCl_3$) species also produce carbonyl dihalide (COX_2) intermediates. In contrast to CF_2Cl_2, CCl_4 and $CDCl_3$, electron-stimulated decomposition of CD_2Cl_2 does not produce a carbonyl dihalide as an intermediate (figure 12). Although specific identification of carbon-containing intermediates produced in the electron-stimulated decomposition of CD_2Cl_2 cannot be made unambiguously, CO_2 is observed to be the final stable carbon-containing product within the film. The formation of CO_2 from CD_2Cl_2 is thought to result from a combination of DEA processes (associated predominantly with C–Cl bond cleavage) and reactions with oxygen-containing species (principally OH radicals) leading to the loss of C–H bonds.

In CH_3I/water (ice) films, evidence of methane is detected in RAIR spectra (figure 12(b), spectrum (vi)) as a product species, presumably as a result of reactions between the $\cdot CH_3$ radical generated in the initial DEA process and surrounding H_2O or CH_3I molecules.

$$\cdot CH_3I + e^- \rightarrow \cdot CH_3 + I^- \tag{10a}$$

$$\cdot CH_3 + H_2O \rightarrow CH_4 + \cdot OH \tag{10b}$$

Downloaded At: 16:25 21 January 2011

In contrast to the other organohalides (CF_2Cl_2, CCl_4, $CDCl_3$ and CD_2Cl_2), electron-stimulated reactions of CH_3I does not produce any hydronium ions (figure 12). This difference is ascribed to the lack of a C–X bond in the methyl radical generated in the DEA to CH_3I. This is believed to preclude the formation of hydronium ions during the reaction of this methyl radical with oxygen-containing species, notably hydroxyl radicals. By contrast, the presence of a C–X bond in the carbon-containing intermediate generated during the initial DEA is correlated with a reaction pathway that leads to the formation of hydroxonium ions. For example, in the case of CCl_4:

$$\cdot CCl_3 + \cdot OH \xrightarrow{H_2O} COCl_2 + H_3O^+ + Cl^- \tag{11}$$

For CH_3I, electron-stimulated reactions also lead to the production of CO_2, illustrating the importance of both C–H and C–X bond cleavage events.

In summary, the reaction pathways of $CDCl_3$, CD_2Cl_2 and CH_3I indicate:

1. The complexity of decomposition pathways for organohalides. The initial step in the reactivity of each organohalide is thought to be dominated by DEA leading to the production of a halide anion and a carbon-containing radical. Thus, for CF_2Cl_2 and CCl_4, the proposed pathways (schemes 1 and 2) are best regarded as a subset of the overall reaction schemes, which incorporate the dominant decomposition pathways for these molecules;
2. The importance of thermodynamic sinks for carbon-containing species in the decomposition pathway, notably $COCl_2$ and CO_2;
3. The importance of reactivity associated with the carbon-containing radical produced in the initial DEA process in determining the overall reaction products. For example, it is the lack of a C–X bond in the $\cdot CH_3$ intermediate that appears to be responsible for the absence of proton production in the electron-stimulated decomposition of CH_3I.

Downloaded At: 16:25 21 January 2011

6. Conclusions

This review has surveyed the electron-driven chemistry of condensed halogenated compounds adsorbed on metal substrates and co-adsorbed with water on metal surfaces, with emphasis on results from the authors' laboratories. Specifically, we focus on the effect of a solvent, H_2O, on the electron-driven chemistry of condensed halogenated compounds. We have demonstrated, using halomethanes (CF_2Cl_2, CCl_4, CH_3I, $CDCl_3$, CD_2Cl_2) and SF_6 as illustrative examples, that medium-energy electrons ($\sim$100 eV) and high-energy photons both induce a broad energy distribution of secondary electrons, which induce the same chemistry in irradiated halocarbon/water films. Indeed, these low-energy secondary electrons ($<$20 eV) are mainly responsible for the rich electron-driven chemistry, which includes molecular decomposition, desorption of negative ions, radical formation and condensed-phase reactions.

We have shown that complex measurements that include different surface science techniques (RAIRS, XPS, TPD, ESD, ESDIAD) can provide a comprehensive description of the surface electron-driven processes. In particular, the ability to make direct measurements of the parent concentration using vibrational spectroscopy (RAIRS) and temperature-programmed desorption methods complements indirect gas-phase measurements of the ESD negative/positive ion yields. We have addressed

some of the concerns raised in a recent report on the state of current understanding of electron-driven processes in water [4, 5]. In brief, our findings can be summarized as follows:

1. Surface analysis tools have been used to probe the structure and dynamics of adsorbate layers on surfaces. With measurements of ESD ion angular distributions (ESDIAD) we are able to determine the geometry of adsorbed SF_6 and CF_2Cl_2 on Ru(0001). TPD has been also used to probe the properties of neat halomethane films ($\leq$10 ML) and halomethanes co-adsorbed with water. The observations emphasize the need for more extensive application of surface analysis tools to probe the structure and dynamics on the surface.
2. We conclude that the decomposition of condensed organohalides induced by low-energy secondary electrons occurs most effectively via a dissociative electron attachment (DEA) mechanism. In a water ice matrix, electron-driven processes result in the formation of stable, solvated anions (F^-, Cl^-) and carbon dioxide (CO_2). Subsequent chemical reactions involving dissociation fragments lead to the production of new carbon-containing species such as carbonyl dihalides COX_2 (X = halogen) and CO_2. We have presented molecular level interpretations of the electron-stimulated reactions of the CF_2Cl_2/water (ice) and CCl_4/water (ice) multicomponent systems. For instance, for CF_2Cl_2/H_2O films we have shown that the product partitioning is dependent on the film's initial composition. In water-rich films CO_2 and COF_2 production is favoured, while in CF_2Cl_2-rich films a thermally stable, partially halogenated polymeric CF_xCl_y film is detected by XPS. The possible non-thermal reaction pathways for several halomethanes co-adsorbed with water have been discussed and compared.
3. The results of *direct* measurements (using TPD) of total dissociation cross-sections for CF_2Cl_2 and CCl_4 adsorbed alone and co-adsorbed with water on a metal surface are compared with recent ESD and charge-trapping experiments that provided *indirect* measurements of DEA cross-sections. In particular, we have shown that the cross-sections for the electron-induced decomposition of CF_2Cl_2 and CCl_4 are similar on the metal surface and increase by factors of 2 to 4 for both molecules in a water (ice) environment. However, the increase is considerably smaller than inferred from previous indirect measurements and possible reasons for the differences are discussed. The highest measured decomposition cross-sections for $\sim$200 eV incident electrons have been observed for fractional monolayer halocarbon coverage on a water ice surface and for very dilute halocarbon/water mixtures: $(1.0\pm0.2) \times 10^{-15}$ cm^2 for CF_2Cl_2 and $(2.5\pm0.2) \times 10^{-15}$ cm^2 for CCl_4.

6.1. *Future directions*

Although this review specifically deals with halogenated compounds, general research into the area electron-stimulated reactions of condensed multicomponent systems is required in the coming years. One of the main challenges is to resolve the reasons behind the discrepancies in the cross-sections obtained from indirect measurements (charge trapping and ESD experiments) and from direct studies (TPD, XPS, IR). In particular, more work needs to be done on the effect of the solvent in determining the magnitude of the cross-section in halogenated compounds. The effects of spacer thickness, solvent polarity (polar vs. non-polar),

Downloaded At: 16:25 21 January 2011

substrate composition and molecular structure (CF_2Cl_2 vs. other CFCs) on the magnitude of the cross-section for dissociation of halogenated species also warrant further investigation.

With the increased levels of sophistication in experimental and computational methods, it is now possible to study systematically mixed component systems. This is particularly important in biological systems where macromolecules in cells are localized in an aqueous environment. Thus, with current theoretical and experimental tools, we can begin to ask questions that transcend the traditional physical science boundaries into biology. For example, Sanche and co-workers have used DFT [132] and scattering theory [133] to model radiation-induced DNA damage. However, further advances in theory are required to account for the role of the solvent (e.g. molecular interactions) and the ensemble of charged and neutral species.

With the increasing interest in confronting biologically relevant problems, surface science methods are among the most powerful tools available to researchers in elucidating the molecular level mechanisms in electron-stimulated reactions. Specifically, there is the need to ask the right questions and use the correct model molecules:

1. What is the mechanism for electron-stimulated bond rupture and where is the excitation localized in complex molecules (e.g. proteins) with multiple reactive centres? How does the presence of a solvent influence the dissociation process and the product species?
2. What are the decomposition fragments? Are there common reaction pathways and mechanisms for a given class of compounds that can offer predictive insights for other molecules? Can we also make predictions based upon theory?

Downloaded At: 16:25 21 January 2011

New developments in instrumentation, such as scanning probe energy loss spectroscopy [134], open the possibility to make use of the advantages of scanning probe and vibrational spectroscopies for localized electron-driven chemistry. The scanning probe enables the reaction that is initiated by electron-tunnelling between the tip and the sample to be 'imaged' in a localized way, as the tunnelling electrons are collected and analysed. In principle, the information from the electron energy loss measurement can provide qualitative and quantitative information on vibrational and electronic resonances and cross-sections. Ideal candidates for this approach could range from bilayer lipid molecules to enzymes, where electron-stimulated reactions can be made site-specific.

Acknowledgements

The Rutgers University work has been supported by the National Science Foundation (NSF), Grant # CHE 0315209; the studies carried out at Johns Hopkins University have also been supported by the NSF, Grant no. CHE-0089168, as part of the Collaborative Research Activities in Environmental Molecular Science in Environmental Redox-Mediated Dehalogenation Chemistry at the Johns Hopkins University. The authors would also like to acknowledge the significant contributions to this work by Glenn Wolfe, Chad Vecitis and Daniela Kusmierek, and Drs Anthony Wagner, Jessica Torres, Qing-Bin Lu, Sergey Solovev and Boris Yakshinsky.

Downloaded At: 16:25 21 January 2011

References

[1] K.H. Becker, C. W. McCurdy, T. M. Orlando and T. N. Rescigno, *Electron-Driven Processes: Scientific Challenges and Technological Opportunities*. (Report of DOE Workshops) 2000. Available at http://attila.stevens-tech.edu/physics/People/Faculty/Becker/EDP.

[2] J. M. White, J. Mol. Catal. A: Chem. **131**, 71 (1998).

[3] J. W. T. Spinks and R. J. Woods, *An Introduction to Radiation Chemistry* (Wiley, New York, 1990).

[4] B. C. Garrett *et al*. *Understanding the Role of Water on Electron-Initiated Processes and Radical Chemistry* (Pacific Northwest National Laboratory, 2003). Available at: http://www.sc.doe.gov/production/bes/chm/Publications/WaterWorkshopReport_final.pdf.

[5] B. C. Garrett *et al*. Chem. Rev. (submitted). Available at: http://www.pnl.gov/waterworkshop/.

[6] R. A. Frosch, Sci. Am. **283**, 180 (1995).

[7] J. P. Barnes and W. A. Bernhard, Radiat. Res. **143**, 85 (1995); R. Chaler, R. Vilanova, M. Santiago-Silver, P. Fernandez and J. O. Grimatt, J. Chromatogr. A **823**, 73 (1998); J. G. Currie and H. Kallio, Lipids **28**, 217 (1993).

[8] M. A. Huels, B. Boudaiffa, P. Cloutier, D. Hunting and L. Sanche, J. Am. Chem. Soc. **125**, 4467 (2003).

[9] T. E. Madey, R. E. Johnson and T. M. Orlando, Surf. Sci. **500**, 838 (2002).

[10] Q. B. Lu and L. Sanche, Phys. Rev. Lett. **87**, 078501/1 (2001).

[11] Q. B. Lu and L. Sanche, Phys. Rev. Lett. **89**, 219801 (2002).

[12] R. Müller, Phys. Rev. Lett. **91**, 058502 (2003).

[13] D. L. Illman, Chem. Eng. News **71**, 9 (1993).

[14] Q. B. Lu and T. E. Madey, J. Chem. Phys. **111**, 2861 (1999).

[15] J. M. Greenberg, Surf. Sci. **500**, 793 (2002).

[16] M. Gwentili, *Nanolithography: A Borderline Between STM, Electron-beam, Ion-beam, and X-ray Lithographies* (Kluwer, Boston, 1994).

[17] K. Mackenzie, F.-D. Kopinke and M. Remmler, Chemosphere **33**, 1495 (1996); G. A. Zacheis, K. A. Gray and P. Kamat, J. Phys. Chem. B **103**, 2142 (1999).

[18] N. Itoh and A. M. Stoneham *Materials Modification by Electronic Excitation* (Cambridge University Press, Cambridge, 2001).

[19] L. Sanche, *Excess Electrons in Dielectric Media* (CRC Press, Boca Raton, FL, 1991), pp. 1–42.

[20] A. D. Bass and L. Sanche, Low Temp. Phys. **29**, 270 (2003); E. Illenberger, Surf. Sci. **528**, 67 (2003).

[21] M. Akbulut, N. J. Sack and T. E. Madey, Surf. Sci. Rep. **28**, 177 (1997).

[22] T. E. Madey, Vacuum **37**, 31 (1987); L. Sanche, J. Phys. B: At. Mol. Opt. Phys. **23**, 1597 (1990).

[23] L. Sanche, Surf. Sci. **451**, 82 (2000).

[24] O. Ingolfsson, F. Weik and E. Illenberger, Int. J. Mass Spectrom. Ion Process. **155**, 1 (1996).

[25] E. Illenberger, Chem. Rev. **92**, 1589 (1992).

[26] D. C. Yee, S. Chauhan, E. Yankelevich, V. Bystritskii and T. K. Wood, Biotechnol. Bioeng. **59**, 438 (1998).

[27] Q. B. Lu, Z. Ma and T. E. Madey, Phys. Rev. B **58**, 16446 (1998).

[28] Q. B. Lu and T. E. Madey, Phys. Rev. Lett. **82**, 4122 (1999).

[29] Q. B. Lu and T. E. Madey, Surf. Rev. Lett. **6**, 313 (1999).

[30] Q. B. Lu and T. E. Madey, Surf. Sci. **451**, 238 (2000).

[31] Q. B. Lu, T. E. Madey, L. Parenteau, F. Weik and L. Sanche, Chem. Phys. Lett. **342**, 1 (2001).

[32] Q. B. Lu and L. Sanche, Phys. Rev. B **63**, 153403 (2001).

[33] Q. B. Lu and T. E. Madey, J. Phys. Chem. B **105**, 2779 (2001).

[34] Q. B. Lu and L. Sanche, J. Chem. Phys. **119**, 2658 (2003).

[35] Q. B. Lu and L. Sanche, J. Chem. Phys. **120**, 2434 (2004).

[36] C. C. Perry, G. M. Wolfe, A. J. Wagner, J. Torres, N. S. Faradzhev, T. E. Madey and D. H. Fairbrother, J. Phys. Chem. B **107**, 12740 (2003).

[37] N. S. Faradzhev, C. C. Perry, D. O. Kusmierek, D. H. Fairbrother and T. E. Madey, J. Chem. Phys (submitted).
[38] A. J. Wagner, C. Vecitis, G. M. Wolfe, C. C. Perry and D. H. Fairbrother, Phys. Chem. Chem. Phys. **4**, 3806 (2002).
[39] A. J. Wagner, C. Vecitis and D. H. Fairbrother, J. Phys. Chem. B **106**, 4432 (2002).
[40] N. S. Faradzhev, D. O. Kusmierek, B. V. Yakshinskiy and T. E. Madey, Low Temp. Phys. **29**, 215 (2003).
[41] N. S. Faradzhev, D. O. Kusmierek, B. V. Yakshinskiy, S. M. Solovev and T. E. Madey, Surf. Sci. **528**, 20 (2003).
[42] *The Handbook of X-ray Photoelectron Spectroscopy*, edited by G. E. Muilenberg (Perkin Elmer Corporation, Eden Prairie, MN, 1979).
[43] L. G. Christophorou, D. L. McCorkie and A. A. Christodoulides, *Electron Molecule Interactions and their Applications* (Academic Press, 1984), Vol. 1.
[44] L. G. Christophorou, D. L. McCorkie and A. A. Christodoulides, Electron Molecule Interactions and their Applications, Vol. 1 (Academic Press, New York, 1984).
[45] S. J. Dixon-Warren, E. T. Jensen and J. C. Polanyi, J. Chem. Phys. **98**, 5938 (1993).
[46] E. Illenberger, H. U. Scheunemann and H. Baumgaertel, Chem. Phys. **37**, 21 (1979).
[47] A. Kiendler, S. Matejcik, J. D. Skalny, A. Stamatovic and T. D. Maerk, J. Phys. B **29**, 6217 (1996).
[48] Y. Wang, L. G. Christophorou and J. K. Verbrugge, J. Chem. Phys. **109**, 8304 (1998).
[49] H. S. W. Massey, *Negative Ions* (Cambridge University Press, London, 1976).
[50] D. Klar, M.-W. Ruf and H. Hotop, Int. J. Mass Spectrom. **205**, 93 (2001).
[51] S. Matejcik, V. Foltin, M. Stano and J. D. Skalny, Int. J. Mass Spectrom. **223–224**, 9 (2003).
[52] P. Rowntree, L. Sanche, L. Parenteau, M. Meinke, F. Weik and E. Illenberger, J. Chem. Phys. **101**, 4248 (1994).
[53] H.-X. Wan, J. H. Moore and J. A. Tossell, J. Chem. Phys. **94**, 1868 (1991).
[54] K. Aflatooni and P. Burrow, J. Chem. Phys. **113**, 1455 (2000).
[55] K. Nagesha, V. R. Marathe and E. Krishnakumar, Int. J. Mass Spectrom. Ion Process. **145**, 89 (1995).
[56] F. Weik and E. Illenberger, J. Chem. Phys. **109**, 6079 (1998).
[57] L. Šiller, N. Vanter and R. E. Palmer, Surf. Sci. **465**, 76 (2000).
[58] L. G. Christophorou and J. K. Olthoff, J. Phys. Chem. Ref. Data **29**, 267 (2000).
[59] L. G. Christophorou and J. K. Olthoff, Int. J. Mass Spectrom. **205**, 27 (2001).
[60] T. Stanski and B. Adamczyk, Int. J. Mass Spectrom. Ion Process. **46**, 31 (1983); D. Margreiter, G. Walder, H. Deutsch, H. U. Poll, C. Winkler, K. Stephan and T. D. Märk, Int. J. Mass Spectrom. Ion Process. **100**, 143 (1990).
[61] M. Meinke, L. Parenteau, P. Rowntree, L. Sanche and E. Illenberger, Chem. Phys. Lett. **205**, 213 (1993).
[62] A. D. Bass and L. Sanche, Radiat. Phys. Chem. **68**, 3 (2003).
[63] X. Y. Zhu, Surf. Sci. **390**, 224 (1997).
[64] X. L. Zhou, X. Y. Zhu and J. M. White, Surf. Sci. Rep. **13**, 73 (1991).
[65] E. P. Marsh, T. L. Gilton, W. Meier, M. R. Schneider and J. P. Cowin, Phys. Rev. Lett. **61**, 2725 (1988); E. P. Marsh, F. L. Tabares, M. R. Schneider, T. L. Gilton, W. Meier and J. P. Cowin, J. Chem. Phys. **92**, 2004 (1990).
[66] Y. Lilach and M. Asscher, J. Chem. Phys. **119**, 407 (2003).
[67] A. Yabushita, Y. Inoue, T. Senga, M. Kawasaki and S. Sato, J. Chem. Phys. B **106**, 3151 (2002); A. Yabushita, M. Kawasaki and S. Sato, J. Phys. Chem. A **107**, 1472 (2003).
[68] M. Meinke, PhD thesis, Institut für Physikalische und Theoretische Chemie, Takustrasse, 1995.
[69] M. N. Hedhili, M. Lachgar, Y. Le Coat, R. Azria, M. Tronc, Q. B. Lu and T. E. Madey, J. Chem. Phys. **114**, 1844 (2001).
[70] S. M. Solovev, D. O. Kusmierek and T. E. Madey, J. Chem. Phys. **120**, 968 (2004).
[71] N. S. Faradzhev, D. O. Kusmierek and T. E. Madey (unpublished work, 2003).
[72] *Excess Electrons in Dielectric Media*, edited by C. Ferradini and J. P. Jay-Gerin (CRC Press, Boca Raton, FL, 1991).
[73] L. Delzeit, B. Rowland and J. P. Devlin, J. Phys. Chem. **97**, 10312 (1993).

Downloaded At: 16:25 21 January 2011

[74] V. P. Zhdanov and P. R. Norton, Surf. Sci. **449**, L228 (2000); V. P. Zhdanov and P. R. Norton, Surf. Sci. **459**, 245 (2000).
[75] M. S. Westley, G. A. Baratta and R. A. Baragiola, J. Chem. Phys. **108**, 3321 (1998).
[76] M. G. Sceats and S. A. Rice, in *Water: A Comprehensive Treatise*, edited by F. Franks (Plenum, New York, 1982), Vol. 7.
[77] K. P. Stevenson, G. A. Kimmel, Z. Dohnálek, R. S. Smith and B. D. Kay, Science **283**, 1505 (1999).
[78] S. Smith and B. D. Kay, Nature **398**, 788 (1999).
[79] D. L. Doering and T. E. Madey, Surf. Sci. **123**, 305 (1982); P. A. Thiel and T. E. Madey, Surf. Sci. Rep. **7**, 211 (1987).
[80] F. T. Mak, S. R. Zele, W. J. Cooper, C. N. Kurucz, T. D. Waite and M. G. Nickelsen, Water Res. **31**, 219 (1997).
[81] T. M. Orlando and G. A. Kimmel, Surf. Sci. **390**, 79 (1997); W. C. Simpson, L. Parenteau, R. S. Smith, L. Sanche and T. M. Orlando, Surf. Sci. **390**, 86; G. A. Kimmel and T. M. Orlando, Phys. Rev. Lett. **77**, 3983 (1996); G. A. Kimmel and T. M. Orlando, Phys. Rev. Lett. **75**, 2606 (1995).
[82] G. A. Kimmel, T. M. Orlando, P. Cloutier and L. Sanche, J. Phys. Chem. B **101**, 6301 (1997); G. A. Kimmel, R. G. Tonkyn and T. M. Orlando, Nucl. Instrum. Methods Phys. Res. B **101**, 179 (1995); G. A. Kimmel, T. M. Orlando, C. Vezina and L. Sanche, J. Chem. Phys. **101**, 3282 (1994).
[83] M. T. Sieger, W. C. Simpson and T. M. Orlando, Nature **394**, 554 (1998).
[84] T. M. Orlando and M. T. Sieger, Surf. Sci. **528**, 1 (2003).
[85] N. G. Petrik and G. A. Kimmel, Phys. Rev. Lett. **90**, 166102/1 (2003).
[86] R. H. Prince, G. N. Sears and F. J. Morgan, J. Chem. Phys. **64**, 3978 (1976).
[87] J. O. Noell, C. F. Melius and R. H. Stulen, Surf. Sci. **115**, 119 (1985).
[88] T. E. Madey, Science **234**, 316 (1986).
[89] M. Akbulut, T. E. Madey, L. Parenteau and L. Sanche, J. Chem. Phys. **105**, 6043 (1996).
[90] J. L. Blanchard and J. T. Roberts, Langmuir **10**, 3303 (1994); X.-L. Zhou and J. P. Cowin, J. Phys. Chem. **100**, 1055 (1996); L. Li, S. Gan, B.-K. Han, H. Qi and R. F. Hicks, Appl. Phys. Lett. **72**, 951 (1998); V. Sadtchenko, K. Knutsen, C. F. Giese and W. R. Gentry, J. Phys. Chem. B **104**, 2511 (2000); C. T. Reeves, R. J. Meyer and C. B. Mullins, J. Mol. Catal. A: Chem. **202**, 135 (2003).
[91] N. J. Sack, L. Nair and T. E. Madey, Surf. Sci. **310**, 63 (1994).
[92] L. Nair, N. J. Sack and T. E. Madey, Nucl. Instr. Methods Phys. Res. B **101**, 79 (1995).
[93] R. S. Smith, C. Huang, E. K. L. Wong and B. D. Kay, Phys. Rev. Lett. **79**, 909 (1997).
[94] K. Adib, N. Camillone III, J. P. Fitts, K. T. Rim, G. W. Flynn, S. A. Joyce and R. M. Osgood Jr., Surf. Sci. **497**, 127 (2002); K. Adib, D. R. Mullins, G. Totir, I. N. Camillone, J. P. Fitts, K. T. Rim, G. W. Flynn and J. R. M. Osgood, Surf. Sci. **524**, 113 (2003).
[95] R. J. Speedy, J. Phys. Chem. **96**, 2322 (1992).
[96] S. E. Stein, in *NIST Mass Spec. Data Center, IR and Mass Spectra in NIST Chemistry WebBook*, NIST Standard Reference Database Number 69, edited by P. J. Linstrom and W. G. Mallard (National Institute of Standards and Technology, Gaithersburg, MD 20899, USA). Available at: http://webbook.nist.gov.
[97] T. Shimanouchi (National Bureau of Standards, 1972), pp. 1–160.
[98] T. Shimanouchi, J. Phys. Chem. Ref. Data **6**, 993 (1977).
[99] S. F. Banham, J. R. Sodeau, A. B. Horn, M. R. S. McCoustra and M. A. Chesters, J. Vac. Sci. Technol. A **14**, 1620 (1996); S. B. Barone, M. A. Zondlo and M. A. Tolbert, J. Phys. Chem. B **103**, 9717 (1999).
[100] S. R. Carlo and V. H. Grassian, J. Phys. Chem. B **104**, 86 (2000).
[101] R. L. Graham, C. D. Bain, H. A. Biebuyck, P. E. Laibinis and G. M. Whitesides, J. Phys. Chem. **97**, 9456 (1993); C. C. Perry, A. J. Wagner and D. H. Fairbrother, Chem. Phys. **280**, 111 (2002).
[102] A. G. Wren, R. W. Phillips and L. U. Tolentino, J. Colloid Interface Sci. **70**, 544 (1979).

Downloaded At: 16:25 21 January 2011

[103] N. J. Sack and T. E. Madey, Surf. Sci. **347**, 367 (1996).
[104] M. D. Alvey, J. T. Yates Jr. and K. J. Uram, J. Chem. Phys. **87**, 7221 (1987).
[105] J. Langer, S. Matt, M. Meinke, P. Tegeder, A. Stamatovic and E. Illenberger, J. Chem. Phys **113**, 11063 (2000).
[106] M. Akbulut and T. E. Madey, *16th Werner Brandt Workshop on Charged Particle Penetration Phenomena*, Oak Ridge, TN, January 7–9, 1996, p. 97; K. A. G. MacNeil and J. C. Tynne, J. Phys. Chem. **74**, 2257 (1970).
[107] M. D. Marshall, K. C. Izqi and J. S. Muenter, J. Chem. Phys. **107**, 1037 (1997).
[108] S. L. Shostak, W. L. Ebenstein and J. S. Muenter, J. Chem. Phys. **94**, 5875 (1991).
[109] *CRC Handbook of Chemistry and Physics*, edited by D. R. Lide (CRC Press, Boca Raton, FL, 1994), p.75.
[110] C. Gahl, U. Bovensiepen, C. Frischkorn and M. Wolf, Phys. Rev. Lett. **89**, 107402 (2002).
[111] J. J. Kaufman, H. E. Popkie and H. J. T. Preston, Int. J. Quantum Chem. **XI**, 1005 (1997).
[112] A. D. Bass, J. Gamache, P. Ayotte and L. Sanche, J. Chem. Phys. **104**, 4258 (1996).
[113] Y. Lilach and M. Asscher, J. Chem. Phys. **117**, 6730 (2002).
[114] T. Livneh, L. Romm and M. Asscher, Surf. Sci. **315**, 250 (1996).
[115] J. Cazaux, Appl. Surf. Sci. **20**, 457 (1985).
[116] V. Cobut, Y. Frongillo, J. P. G. Patau, M.-J. Fraser and J.-P. Jay-Gerin, Radiat. Phys. Chem. **51**, 229 (1998).
[117] J. C. Ashley, J. C. Tung and R. H. Ritchie, IEEE Trans. Nucl. Sci. **NS-26**, 1566 (1978); J. C. Ashley, J. C. Tung, R. H. Ritchie and V. E. Anderson, IEEE Trans. Nucl. Sci. **NS-23**, 1833 (1976); A. Cole, Radiat. Res. **38**, 7 (1969); C. J. Powell and A. Jablonski, Surf. Interface Anal. **33**, 211 (2002); C. J. Powell and A. Jablonski, J. Phys. Chem. Ref. Data **28**, 9 (1999); R. L. Kurtz, N. Ususki, R. Stockbauer and T. E. Madey, J. Electron Spectrosc. Relat. Phenom. **40**, 35 (1986).
[118] R. E. Buehler, in *The Chemistry of the Carbon–Halogen Bond*, edited by S. Patai (Wiley, Chichester, 1973), Part 2, pp. 795–864.
[119] H. Sambe, D. E. Ramaker, L. Parenteau and L. Sanche, Phys. Rev. Lett. **59**, 236 (1987). Preprint available at http://www.physik.fu-berlin.de/%7kfemtoweb/newfemtos/docs/preprints/2004/BGS04.pdf.
[120] M. Akbulut, T. E. Madey and P. Nordlander, J. Chem. Phys. **106**, 2801 (1997).
[121] U. Bovensiepen, C. Gahl, J. Stahler, P. A. Loukakos and M. Wolf, Isr. J. Chem. (submitted).
[122] A. A. Stolov, W. A. Herrebout and B. J. Van der Veken, J. Mol. Struct. **481**, 499 (1999).
[123] S. J. Dixon-Warren, E. T. Jensen and J. C. Polanyi, Phys. Rev. Lett. **67**, 2395 (1991).
[124] M. W. Chase Jr., J. Phys. Chem. Ref. Data **9**, 1 (1998).
[125] V. I. Feldman, F. F. Sukhov, N. A. Slovokhotova and V. P. Bazov, Radiat. Phys. Chem. **48**, 261 (1996).
[126] P. Swiderek, M. C. Deschamps, M. Michaud and L. Sanche, J. Phys. Chem. B **107**, 563 (2003).
[127] N. Nakayama, E. E. Ferrenz, D. R. Ostling, A. S. Nichols, J. F. Faulk and C. R. Arumainayagam, J. Chem. Phys. B **108**, 4080 (2004).
[128] J. J. Russell, J. A. Seetula, D. Gutman, F. Danis, E. Caralp, P. D. Lightfoot, R. Lesclaux, C. F. Melius and S. M. Senkan, J. Phys. Chem. **94**, 3277 (2000).
[129] B. M. Penetrante, M. C. Hsiao, J. N. Bardsley, B. T. Merritt, G. E. Vogtlin, A. Kuthi, C. P. Burkhart and J. R. Bayless, Plasma Sources Sci. Technol. **6**, 251 (1997).
[130] J. Monig, D. Bahnemann and K.-D. Asmus, Chem. Biol. Interact. **47**, 15 (1983).
[131] N. Getoff, Water Res. **20**, 1261 (1996).
[132] X. Li, M. D. Sevilla and L. Sanche, J. Am. Chem. Soc. **125**, 8916 (2003); X. Li, M. D. Sevilla and L. Sanche, J. Am. Chem. Soc. **125**, 13668 (2003).
[133] L. G. Caron and L. Sanche, Phys. Rev. Lett. **91**, 113201/1 (2003).
[134] L. J. Lauhon and W. Ho, Surf. Sci. **451**, 219 (2000); R. E. Palme B. J. Eves, F. Festy and K. Svensson, Surf. Sci. **502–503**, 224 (2002).

Downloaded At: 16:25 21 January 2011